Synoptic scale variability of surface winds and ocean response to atmospheric forcing in the eastern Austral Pacific Ocean

Iván Pérez-Santos[1, 2], Romanet Seguel[2, 3, 4], Wolfgang Schneider[5, 6], Pamela Linford[7], David Donoso[5-8], Eduardo Navarro[3-6], Constanza Amaya-Cárcamo[9], Elías Pinilla[4], Giovanni Daneri[10].

[1]Centro i-mar de la Universidad de los Lagos, Puerto Montt, Chile
[2]Centro de Investigación Oceanográfica COPAS Sur-Austral, Universidad de Concepción, Chile
[3]Programa de Postgrado en Oceanografía, Departamento de Oceanografía, Universidad de Concepción, Chile
[4]Instituto de Fomento Pesquero, Aysén, Chile
[5]Departamento de Oceanografía, Campus Concepción, Universidad de Concepción, Chile
[6]Millennium Institute of Oceanography (IMO), University of Concepción, Chile
[7]Programa de Doctorado en Ciencias mención Conservación y Manejo de Recursos Naturales, Centro i-mar, Universidad de Los Lagos, Puerto Montt, Chile.
[8]Pontificia Universidad Católica de Valparaíso, Chile.
[9]Departamento de Geofísica, Universidad de Concepción, Chile.
[10]Centro de Investigaciones en Ecosistemas de la Patagonia, Coyhaique, Chile.

**Corresponding author: Iván Pérez-Santos: ivan.perez@ulagos.cl*

Abstract. In the southern hemisphere, macroscale atmospheric systems such as the westerly winds and Southeast Pacific Subtropical anti-cyclone (SPSA) influence the wind regime of the eastern Austral Pacific Ocean. The average and seasonal behaviors of these systems are well-known, although wind variability at different time and distance scales remains largely unexamined. Therefore, the main goal of this study was, therefore, to determine the space and time scale variabilities of surface winds from 40° to 56° S, using QuikSCAT, ASCAT, and ERA5 reanalysis surface wind information, complemented by in situ meteorological data. In addition, interactions between atmospheric systems, together with the ocean-atmosphere response, were evaluated, from 1999 to 2018. The empirical orthogonal function detected dominance at the synoptic scale in mode 1, representing approximately 30 % of the total variance. In this mode, low and high atmospheric pressure systems characterized wind variability, with a cycle length of 16.5 days. Initially, mode 2, representing approximately 22 % of the variance, was represented by winds from the west/east direction (43° to 56° S), occurring mostly during spring-summer/fall-winter, with an annual time scale (1999–2008), until they were replaced by systems cycling at 27.5 days (2008–2015), reflecting the influence of the Southern Hemisphere´s baroclinic annular mode. Mode 3, representing approximately 15 % of the variance, involved passage of small scale, low and high atmospheric pressure (LAP, HAP) systems throughout Patagonia. Persistent Ekman suction south of the Gulf of Penas, and up to and beyond the Pacific mouth of the Magellan Strait, occurred throughout the year. Easterly Ekman transport (ET) piled these upwelled waters onto the western shore of South America, when the winds blew southward. These physical mechanisms were essential in bringing nutrients to the surface, and then transporting planktonic organisms from the oceanic zone into Patagonian fjords and channels. In a variation, between 41° and 43° S, upward Ekman pumping dominated the total Ekman

transport instead the ET during spring and summer, causing reduced sea surface temperature, and increased chlorophyll-a; this is the first time that such Ekman upwelling conditions have been reported so far south, in the eastern Pacific Ocean. The influence of northward migrating LAP systems on the ocean-atmosphere interphase allowed us to understand, for the first time, their direct relationship with recorded night time air temperature maxima (locally referred to as "Nighttime heat wave events"). In the context of global climate change, greater attention should be paid to these processes, based on their possible impact on the rate of glacier melting, and on the Austral climate.

Keywords: Atmospheric pressure systems, Ekman upwelling, Pacific Ocean, Patagonia, synoptic scale

1. Introduction

The eastern Austral Pacific Ocean (40° to56° S) is under the influence of westerly winds, and the Southeast Pacific Subtropical anti-cyclone (SPSA) (Tomczak and Godfrey, 1994; Stewart, 2002). In this region, westerly winds are stronger than those in the northern hemisphere, on average, and extend in a belt from 40° to 60° S (Talley et al., 2011). The SPSA shows an annual migration, reaching its southern position (~40° to 46° S) in the Austral summer, owing to the poleward displacement of the intertropical convergence zone (Rahn and Garreaud, 2013; Ancapichun and Garcés-Vargas, 2015; Schneider et al., 2017). The anti-clockwise rotation of winds from the SPSA generates northerly winds along the coastline of Chile and Peru, contributing to the maintenance of upwelling conditions all year around, giving rise to one of the higher productivity marine ecosystems in the world's oceans (Kampf and Chapman, 2016). The system is well known for the contribution of westerly winds and SPSA to the circulation regimen, e.g., formation of the Humboldt Current system (Thiel et al., 2007; Fuenzalida et al., 2008).

While most studies have focused on SPSA behavior (Rahn and Garreaud, 2013; Ancapichun and Garcés-Vargas, 2015; Schneider et al., 2017), and the effect of the ocean-atmospheric interaction, little is known about the surface wind variability in the eastern Austral Pacific Ocean. Therefore, the principal goal of this study was to determine the space and time variability of the surface winds that extend from 40° S to 56° S, using different satellite wind products, reanalysis climates date set, and in situ meteorological information. The interaction between the Austral Pacific surface wind regimen and the SPSA was also taken into account, together with ocean-atmosphere dynamics.

The principal hypotheses of our study were: (1) the passage of synoptic-scale atmospheric events throughout the eastern Austral Pacific Ocean, such as low/high atmospheric pressure (LAP and HAP) systems, dominated the surface wind variations in the study area. (2) The interaction between synoptic scale atmospheric events, such as the SPSA, with LAP systems, allowed the advection of warm air over Patagonia, creating maximum surface air temperatures at nighttime, especially in fall and winter.

In terms of time-distance scales, atmospheric systems have been categorized as macro-, meso-, and microscale (Orlanski, 1975; Ray, 1986; Holton, 1992). The macroscale definition is divided into planetary and synoptic scales. Winds that impact the globe belong to the planetary scale, such as the westerly and trade winds, and also El Niño (Tomasz, 2014), extending over distances from 1000–40000 km, with time scales of weeks or longer. Synoptic scale systems cover 100-5000 km or so, in a timescale of days to weeks, and include events such as atmospheric pressure systems, like subtropical anti-cyclones and hurricanes. Mesoscale events cover a distance and time scale of 1−100 km, in minutes to hours, and include events such as thunderstorms, tornadoes, and sea/land breezes, while microscale systems cover a range of <1 km, and include events such as turbulence, dust devils and gusts, occurring in seconds to minutes. In this manuscript, we evaluated the oceanic response to synoptic scale atmospheric events, including LAP and HAP systems. From meteorological point of view, in a LAP system winds rotate clockwise (southern hemisphere) around a core of low pressure, and are generally associated with severe weather conditions, e.g., intense wind, rain, and cloudy. In contrast, in a HAP system winds rotate counterclockwise (southern hemisphere), and high pressure is located in the center of the event, producing mostly good weather conditions with clear skies.

The passage of LAP events throughout Patagonian fjords and channels, such as Puyuhuapi Fjord, creates intense vertical mixing that favors microalgal blooms, increasing primary production during the winter season to reach a magnitude similar to the traditionally productive spring-summer season (Montero et al., 2017). In the case of HAP events, which produce alongshore winds (northward), the contribution to the upwelling conditions (offshore Ekman transport) in the northern part of the eastern Austral Pacific coastline have not been quantified. Similarly, LAP systems also produce alongshore winds, although in the opposite direction (southward), and favor downwelling; the mechanisms and effects of these events are addressed in Sect. 3.2.

In the California upwelling systems (32°-44° N), the contribution of Ekman transport (ET) and Ekman pumping (EP), with upward velocities favoring upwelling and primary production, and downward velocities contributing to downwelling, were quantified using an atmospheric model, finding that EP was more important than ET (Pickett and Paduan, 2003). In the central-northern region of Chile, where only ET has been evaluated previously as the leading contributor to upwelling, (Sobarzo and Djurfeldt, 2004), one study (Bravo et al., 2016) have demonstrated that EP contributed 40-60 % of the total upwelling transport. ET and EP, derived here using surface wind products from the QuikSCAT and ASCAT satellites and ERA5 reanalysis climate data set, were used in this study to quantify the contribution of these processes to the total upwelling, with special attention to the offshore region of Chiloe Island (42°-43.5° S), where northward wind occurs during spring-summer, due to the SPSA influence.

In this manuscript, statistical analyses, including empirical orthogonal function (EOF) using the surface wind products from the QuikSCAT and ASCAT satellites and ERA5 reanalysis from 1999‒2015, allowed for the estimation of the importance of synoptic scale events in the wind variability of the eastern Austral Pacific Ocean. In addition, the ocean-atmosphere response to the surface wind was evaluated using reanalysis data to the present day, together with a time series of chlorophyll-a, fluorescence and sea surface temperature data from MODIS-Aqua satellite. Air temperature and atmospheric pressure from ERA5 and in-situ data from buoy and meteorological stations were also included in the analyses.

2. Materials and methods

2.1 Satellite and reanalysis surface wind data

Surface wind data was obtained from SeaWinds scatterometers, mounted on the QuikSCAT and ASCAT satellites. QuikSCAT wind vectors were obtained daily, for a 0.5° × 0.5° grid (http://www.ifremer.fr). The root mean square errors (RMSE) for wind velocity and direction were specified to be less than 1.9 m s^{-1} and 17°, respectively (Piolle and Bentamy, 2002). Analysis of QuikSCAT satellite wind data covered the period from July 1999 to November 2009. For the ASCAT wind product, the temporal resolution was also daily-averaged, and the spatial resolution was 0.25° × 0.25° over two swaths with widths of 550 km (Bentamy et al., 2008). The ASCAT data was validated with moored buoys from the National Data Buoy Center (NDBC), MF-UK (Météo-France and UK Met office), TAO buoys, QuikSCAT scatterometers, and the European Centre for Medium-Range Weather Forecasts (ECMWF). Comparison between ASCAT and QuikSCAT data demonstrated good agreement at a wind speed range of 3–20 m s^{-1}, but outside this range, ASCAT underestimated the wind speed. The RMS was not uniform worldwide, with values of 1.5–3.5 m s^{-1}at high latitudes with an average global RMS of 2 m $s^{-1}$from wind direction of 18° (Bentamy et al., 2008).Furthermore, comparison of ASCAT wind fields with data from moored buoys showed correlation coefficients of 0.86 with an RMS of 2 m s^{-1} (Bentamy and Croize-Fillon, 2011). In this study the ASCAT product was used during period from April 2007 to December 2015.

The ERA5 reanalysis climate date set of surface wind was added to the manuscript because it offered continued surface wind data with high temporal and spatial resolution from 1979 to the present day (https://cds.climate.copernicus.eu). Data covering the period from 1999 to 2018 was included. The ERA5 reanalysis used 4D-Var data assimilation in CY41R2 from the ECMWF with 137 levels in the vertical and the top level at 0.01 hPa. This data set is available in hourly temporal resolution with a regular spatial grid of 0.25° × 0.25°. Hourly surface wind data was averaged daily for the analyses presented in Figures 2–10. As surface wind input, ERA5 incorporated different satellite scatterometer data such as, e.g., AMI (ERS 1 and ERS2), ASCAT (METOP-A/B), OSCAT (OCEANSAT-2), and SeaWinds (QuikSCAT). Furthermore, in situ data provided by the World Meteorological Organization information system (WMO-WIS), e.g., land stations, drifting buoys, ship stations, radiosondes, radars, and aircraft data, was added. To understand the origin and influence of the "nighttime heat wave events" in Patagonia, the air temperature (2 m) and surface atmospheric pressure from ERA5 with hourly temporal resolution were utilized.

Local and regional validation process analyses were performed using information from Navy lighthouses (NLHs) located in the coastal zone (Fig. 1). The information from NLHs covered the period from 2009−2011 and 2014, a period where QuikSCAT, ASCAT, and ERA5 surface wind product coincided in operation. Additionally, data from an oceanographic buoy moored in Reloncaví sound (Fig. 1) was used for comparison with ERA5 reanalysis from 2017–2018. As a validation tool, a Taylor diagram was applied to all data sets (Taylor, 2001). In general the validation between satellites and reanalysis surface wind products with the in-situ wind data demonstrated satisfactory results, with correlation coefficients of 0.5–0.9, as well as RMS and standard deviations of ~2–4 m s^{-1}.

The ERA5 showed the highest statistical results (See Supplementary Material for further details regarding the validation process).

2.2 Environmental data from buoys and meteorological stations

Data from an oceanographic buoy installed in the northern section of Puyuhuapi Fjord (Fig. 1, 44° 35.3' S, 72° 43.6' W), and equipped with atmospheric (wind speed and direction, air temperature, and atmospheric pressure), and surface water (temperature and conductivity) sensors, was used to understand fjord-atmosphere interactions. The raw atmospheric data from the buoy were collected with a temporal resolution of 3 min, and the water data were registered hourly at depth of ~1 m. The time series from the oceanographic buoy started in April 2011 and finished in July 2013. A meteorological station was installed on the coast ~500 m from the buoy, to continue atmospheric measurements in this region. The meteorological station registered raw atmospheric data every 15 min (wind speed and direction, air temperature, and atmospheric pressure) from April 2014 to August 2017. Generally, all the atmospheric data was temporally homogenized, from the buoy and the data from the meteorological stations were averaged hourly.

2.3 Satellite derived sea surface temperature, chlorophyll-a, and fluorescence data

Satellite-derived images and time series of chlorophyll-a (Chl-a) concentration, normalized fluorescence line height (FLH) and sea surface temperature (SST) were obtained from the Moderate Resolution Imaging Spectroradiometer (MODIS) sensor, on the Aqua satellite. The data were obtained with a spatial resolution of 4 km^2 per pixel, at nadir, over cloud-free ocean areas, with a temporal resolution of 8 days, covering the period from 2002–2018. Chl-a, FLH and SST images and time series were extracted from the Geospatial Interactive Online Visualization and Analysis Infrastructure (Giovanni; https://giovanni.gsfc.nasa.gov), and were used as measures of the marine response to the surface winds, and the associated processes, e.g., ET and EP.

2.4 Derived variables

The influence of surface wind on the ocean response was monitored throughout the calculation of the ET and EP. Both processes participate in the injection of nutrients from the deep layer to euphotic zone, where the phytoplankton are more abundant, increasing primary production (Thurman and Trujillo, 2004). In the ET, wind blowing to the equator (Polar) on the western coastline generates an offshore (onshore) mass transport to the ocean, causing the upwelling (downwelling) of rich water. In contrast, EP originates from the divergence (convergence) of wind stress curl, contributing to the upwelling (downwelling) of water due to the positive (upward) and negative (downward) EP velocities (Tomczak and Godfrey, 1994; Stewart, 2002).

Using QuikSCAT and ASCAT surface wind data, the components of the zonal and meridional wind stress (τ_u and τ_v, respectively), were calculated, as shown in Eq. (1).

$$\tau_u = \rho_a C_d u U_{10},\ \tau_v = \rho_a C_d v U_{10} \quad (1)$$

In Eq. (1), ρ_a is air density (1.2 kg m^{-3}), C_d is a dimension less drag coefficient; *u* and *v* are the zonal and meridional wind components, respectively; and U_{10} is the magnitude of the wind vector 10 m above sea level. C_d was calculated using the formula proposed by Yelland and Taylor (1996), in which the coefficient varies as a function of the wind velocity, according to Eqs. (2 and 3).

$$C_d = 0.29 + \frac{3.1}{U_{10}} + \frac{7.7}{U^2{}_{10}} \times 10^{-3}, \text{ for } U_{10} \leq 6ms^{-1} \quad (2)$$

$$C_d = 0.60 + 0.070U_{10} \times 10^{-3}, \text{ for } 6ms^{-1} \leq U_{10} \leq 26ms^{-1} \quad (3)$$

Ekman surface transport, M (m^2 s^{-1}), was calculated for each grid point of the satellite wind field using Eq. (4) (Smith, 1968).

$$\vec{M} = \frac{\vec{\tau}}{\rho_w f} \quad (4)$$

In Eq. (4), $\vec{\tau}$ is the wind stress vector, ρ_w is the water density (1025 kg m^{-3}), and f is the Coriolis parameter. The EP velocity, W_E (m^3 s $^{-1}$), was calculated according to Eq. (5) (Smith, 1968).

$$W_E = \frac{1}{\rho_w f} \nabla \times \vec{\tau} \quad (5)$$

In Eq. (5), $\nabla \times \vec{\tau}$ is the wind stress curl, which was derived by first order cross-differencing of the wind stress field, which implies that no curl computation was possible for the grid points nearest to the coast. This drawback was overcome by applying coKriging, in two dimensions, to the wind stress curl, which allowed extrapolation toward the coast (Marcotte, 1991).

To quantify the relative importance of EP for the total upwelling transport (TUT), EP velocities were integrated up to ~50 km offshore along three transects located in the northern (42.7° S), central (47.2° S), and southern (52.0° S) parts of the study region (Fig. 1). This calculation was performed to obtain the vertical transport (m^3 s^{-1}) for each selected transect, and compare it with the ET obtained by Eq. (4), following the methodology proposed by Pickett and Paduan (2003). In Fig. 11 TUT was averaged every 8 days for comparison with the MODIS-Aqua variables, e.g., Chl-a, FLH and SST.

2.5 Data analysis

Zonal and meridional surface winds from QuikSCAT (1999–2009), ASCAT (2007–2015) and ERA5 reanalysis (1999–2015), were used to apply EOF analysis (Emery and Thomson, 1998; Kaihatu et al., 1998), to determine the modes of variability that dominated the spatiotemporal behavior of the wind field in the eastern Austral Pacific Ocean. Before computing the EOFs, long term means and linear trends were removed for each scatterometer (QuikSCAT and ASCAT) and reanalysis product (ERA5) separately. To complete this process, the mean and linear trend calculations were applied to all grid points covering the entire data set period.

A Morlet wavelet analysis was applied (Torrence and Compo, 1998) to the time-dependent coefficients of the three leading modes, resulting from real-vector EOF analysis of the QuikSCAT, ASCAT and ERA5 reanalysis surface wind fields. This wavelet analysis allowed for the distinction of time and duration of the dominant periods of the different atmospheric processes. The wavelet spectra were used to calculate the time-averaged spectra for the entire sampling period, and are subsequently referred to as the global wavelet spectrum (Torrence and Compo, 1998).

3. Results

3.1 Surface wind features and variability

Analysis of the surface wind long term daily mean, for the period 1999-2015, using the QuikSCAT and ASCAT satellite products and the ERA5 reanalysis climate data set, showed similar patterns (Fig. 2). In general, westerlies were the predominant the surface winds, especially between 42° and 45° S, although a more detailed analysis indicated different features. 1) North of 42° S, the wind was slightly west-southwesterly. 2) South to the 45° S, the wind started an inclination from the west to the northwest direction, and 3) between the 52° S and 56° S, the wind blew along the Austral coast of the Magellan region, while in the rest of the study area, the wind direction was perpendicular to the coast. The surface wind average registered as a meridional gradient, in which low speeds (5–6 m s^{-1}) were observed in the northern domain, and stronger wind (10–2 m s^{-1}) was registered down towards 51° S. The standard deviations were very similar between satellite products (±3.0 to ±4.2 m s^{-1}), representing the same meridional gradient observed in the surface wind magnitude, but the ASCAT data registered lower variability and less intense surface wind magnitudes, compared with the data obtained by QuikSCAT (Figs. 2a and 2b). Nevertheless, lower standard deviations and wind magnitudes were obtained by the ERA5 reanalysis data (Fig. 2c). Computation of the seasonal cycle, using all datasets e.g., QuikSCAT, ASCAT and ERA5, showed a similar meridional gradient to that obtained in the average analysis, highlighting the time-persistence and high intensity of the northwesterly winds in the open ocean water of the Magellan region (51° to 56° S).

EOF analysis allowed further understanding of the surface wind variability modes, and distribution of the total variance. The EOF for the QuikSCAT (1999–2009) daily data showed a concentration of ~70 % of the total variance in the first three empirical modes: EOF-1=30.01 %; EOF-2=22.5 %; EOF-3=16.4 % (Fig. 3a–c). For the equivalent ASCAT (2007–2015) daily wind data, the EOF represented ~65 % of the total variance, in the first three empirical modes: EOF-1=27.9 %; EOF-2=22.5 %; EOF-3=15.3 % (Fig. 3d–f). In contrast, the ERA5 reanalysis data showed similar variance, but covered the total sampling period with EOF-1=28.6 %, EOF-2=25.9 % and EOF-3=18.2 % (Fig. 3g–i). The spatial structure of the first three modes from the QuikSCAT, ASCAT and ERA5 databases were similar (Fig. 3). In terms of the spatial structure of mode 1 (Fig. 3a, d and g), southerly and southwesterly winds dominated the study area when the time-dependent coefficient was positive (Figs. 4a, 5a and 6a, PC-1). When principal component 1 (PC-1) was negative, the spatial structure of mode 1 rotated, and northerly and northeasterly winds occurred.

The global spectrum analysis performed for PC-1 denoted the dominant, 16.5 days cycle (Fig. 4b and 5b). The PC-1 monthly mean calculation demonstrated that southerly winds occurred mostly during the fall and spring, while northerly winds were more frequent during winter, spring, and summer (Fig. 4c and 5c). The global spectrum of the complete and continuous data set of the ERA5 reanalysis again showed the 16.5 days cycle and the annual cycle, which was approximately 314 days (Fig. 6b). For the monthly mean calculation, an alternating dominance of southerly and northerly winds was observed (Fig. 6c). The southerly and northerly winds were associated with the passage of intense HAP (Fig. 7a) and LAP (Fig. 7b) systems, throughout the study region.

The spatial structure of mode 2 highlights the presence of the easterly (positive time-dependent coefficient), and westerly winds (negative time-dependent coefficient) (Fig. 3b, 3e and 3h). The global spectrum for the PC-2 (Fig. 4d and 4e) represented the dominance of the annual cycle of 374 days for the QuikSCAT database. The low pass filtered time series for the PC-2 (Fig. 4d, red line) showed the occurrence of the most positive values during the fall and winter season, represented by the easterly winds (Fig. 4f). The negative part of the PC-2 was observed during spring and summer, highlighting the presence of the westerly winds (Fig. 4f). Even though the spatial structure of mode 2 from the ASCAT database presented a similar pattern to the QuikSCAT mode 2, the annual cycle period was not detected in the spectrum of PC-2 (Fig. 5d and 5e). In this analysis, cycles of 27.5 days and 16.5 days were obtained. The monthly mean for PC-2 coincided with the results from QuikSCAT during winter (easterly winds), and spring (westerly winds), but was different in summer and fall, where the wind direction varied (Fig. 5f). PC-2, the global spectrum signal and monthly mean calculations obtained using the ERA5 data reflected a combination of results registered with the QuikSCAT and ASCAT data sets, highlighting the dominance of the 374 and 27.8 days cycles (Fig. 6d–f). Figures 7c and 7d shows examples of the atmospheric systems involved in the wind direction variability characteristic of this mode.

The spatial structure of mode 3 can be represented by a clockwise atmospheric circulation (e.g., Fig. 7e) of surface winds, in the same direction as LAP system when the time-dependent coefficient was positive (Figs. 3c, 3f and 3i). The rotation of the winds became counterclockwise (e.g., Fig. 7f) when the time-dependent coefficient was negative, representing a structure similar to that seen for an HAP system (Figs. 4g, 5g and 6g). Periods of 2–8 days were detected in the spectrum analysis of all data sets (QuikSCAT, ASCAT and ERA5), while semiannual (157 days) and annual cycles were also observed (Figs. 4h-i, 5h–I and 6h–i).

Wavelet analysis facilitated the observation of the year-round dominance of the synoptic time scale obtained by PC-1 (Fig. 8a and 8b). An evident change in time scales was observed for PC-2, e.g., the annual cycle dominated from 2000–2008 (Fig. 8c), but from 2009–2015, a 20–30 day cycle was more intense than the annual cycle (Fig. 8d). In PC-3, the semiannual signal observed in the global spectrum (Fig. 4h) occurred during 2004 (Fig. 8e). However, while the annual cycle registered in Fig. 5h, was clear in 2011 (Fig. 8f), synoptic time scales were persistent from 2000-2015 (Fig. 8e and 8f). The wavelet analysis performed on the ERA5 PC-1, PC-2 and PC-3 (Fig. 8g–i) confirmed the results obtained from the QuikSCAT and ASCAT data sets, showing the change in time scales registered in PC-2 starting in 2009, and higher energies from the annual cycle from 1999 to 2006.

3.2 Derived parameters from surface winds and ocean implications

The average dominance of the westerly surface wind stress generally produced a northerly Ekman transport (ET) in the study region (Fig. 9a–c). On average, the ET ran parallel to the coast, between 40° and 47° S, and from there to 56° S, the inclination of the coastline, and the influence of the westerly wind stress, contributed to change the ET direction, orienting mostly perpendicular to the coast. This was the region (48° to 56° S), where the highest ET value (2.16 m^2 s^{-1}) was recorded, due to the presence of the most intense regional winds (Fig. 2). Moreover, a wide area of positive (upward motion), and maximum Ekman pumping (EP=0.25 m day^{-1}), was observed approximately 51° S, in the QuikSCAT data and the positive EP extended across the study area (Fig. 9a).The same area of positive and intense EP was observed in the ASCAT database, although in the northern part of the study region, between 40° and 48° S, the upward EP was located closer to the coast, covering approximately the first ~100 km (Fig. 9b). The long term mean of daily ET and EP calculated with ERA5 was similar to that obtained for the QuikSCAT period showing the greatest coincidences with areas where EP was maximized (Fig. 9c). However, the ERA5 values were the higher with EP=0.57 m day^{-1} at 50.5° S / 76.25° W. Moreover, EP was also high in the ERA5 dataset along the coastline between 40° S to 44° S (Fig. 9).

The analysis (from Fig.2–9) using the satellite wind surface products, QuikSCAT and ASCAT, together with the reanalysis product demonstrated that ERA5 showed stronger similarities between the results. Hence, in order to understand the annual variability of the ET and EP, and the contribution of both processes to the total upwelling transport (TUT), three data time series from ERA5 were extracted, for the northern, central and southern parts of the study region, covering1999–2018 (Fig. 10). In the northern part of the study region, in ocean water as the coast of Chiloe Island, the long term TUT daily mean showed high variability (±0.82 m^3 s^{-1}) year-round, especially during fall and winter, when onshore ET dominated the TUT. This condition changed during part of the spring and all the entire summer, showing mainly offshore ET, but with a weaker magnitude than that observed during winter. The EP was positive, and dominated the TUT (Fig. 10a). The long term, monthly mean of the time series showed the dominance of downwelling conditions, from May to October (Austral fall-winter). The upwelling typically began in November and finished in April, with a significant contribution from the EP (Fig. 10b). The cumulative transport was in generally favorable to downwelling, from May to December, with reduced upwelling in the summer (Fig. 10c).

In the time series data for the Gulf of Penas, the year-round variability of the long term daily TUT mean was observed (±0.97 m^3 s^{-1}), but the offshore ET events decreased, and EP showed reduced positive values (Fig. 10d). Downwelling conditions prevailed, due to the dominance of the ET during the year (Fig. 10e) and the cumulative transport was negative (downwelling) for ET and TUT and higher than observed in the northern time series (Fig. 10f).

In the southern part of the study region, close to the entrance of the Magellan Strait, the absolute maximum (-8.25 m^3 s^{-1}) was reported, along with higher variability of the TUT (±1.24 m^3 s^{-1}), which was dominated by the ET. The EP was positive and favorable for upwelling, but less intense than for the ET (Fig. 10h). The long term monthly mean for transport showed the highest values for the ET, and the highest contribution of this process to the TUT, even though the EP was positive and favorable for upwelling (Fig. 10i). The cumulative transport was also the most important, compared with the other time series (Fig. 10j).

Downwelling conditions generally dominated the study region, but in the open ocean water around Chiloe Island, upwelling was observed during spring-summer owing to the contribution of the wind stress curl that generated positive EP velocities. Considering the previous results showing that surface winds (ET and EP) contributed to the injection of subsurface water to the surface layer, the time series of TUT together with satellite Chl-a, FLH and SST were used to evaluate the oceanic response during favorable upwelling conditions (Fig. 11).The time series of TUT from 2002 to 2018 showed an annual cycle where upwelling conditions occurred during spring-summer (Fig. 11a, red shaded area), while downwelling conditions were typically observed in fall and winter (Fig. 11a, blue shaded area). The anomalies of Chl-a showed a positive response to the TUT (Fig. 11b) with a correlation coefficient (Corr. coef.) of 0.32. Because the Chl-a signal was contaminated with suspended solid sediments and other non-biological signals, FLH time series was incorporated into the analysis, showing a Corr. Coef. of 0.54 with Chl-a. In this case, FLH also exhibited a positive relationship with TUT with a Corr. coef. of 0.27 (Fig. 11c). Negative SST anomalies were also observed during fall and winter and at lower frequency during the spring and summer compared to that of the upwelling response (Fig. 11d). The Corr. coef. between the SST anomalies and TUT was 0.29. From an inter-annual point of view, a high amount of positive anomalies of Chl-a and FHL was observed, e.g., 2008, 2014, and 2016 and in the SST anomalies of 2004, 2008–2009, and 2016–2017. For the TUT time series, no inter-annual variability was observed, but from 2017 to the end of 2018, decreasing amounts of positive TUT was observed. The SST (Fig. 11e and g) and Chl-a images (Fig. 11f and h) obtained during the upwelling provided evidence of the oceanic response to the TUT. Along the west coast of Chiloe Island, the SST dropped by approximately 4°C and the Chl-a increased ~10–15 mg m^{-3} compared with the values in the open Pacific Ocean waters. These examples demonstrated the importance of TUT in the oceanic response to wind.

3.3 Relationship of synoptic events with nighttime heat waves

The long term hourly mean of the surface air temperature (SAT) obtained from buoy and meteorological station data showed the same patterns with a markedly diurnal cycle, where the SAT maximum was registered in the afternoon (15:00–18:00, local time), while absolute minima were observed early in the morning (6:00–8:00; Fig. 12a and d). The observed SAT diurnal cycle coincided with the solar radiation maximum moment, as shown in the net solar radiation time series from the buoy and meteorological station (Fig. 12b and e).The spectral analysis of both time series (SAT and net solar radiation) showed the dominance of the diurnal cycle (24 h) followed by the semidiurnal cycle (12 h; Fig. 12c and f). The histogram of the SAT absolute maxima demonstrated a bimodal structure, with an initial peak in the afternoon, as was observed in the diurnal cycle (Fig. 12a and d) and a second peak at night from ~21:00 to 05:00 (Fig. 12g and h). The first peak can be described by solar radiation and the balance of this subsection describes the processes involved in the SAT nighttime maximum, known in this manuscript as "nighttime heat wave events".

The time series registered 236 nighttime heat wave eventsfrom2011 to 2017 (Fig. 13a).On average, ~46 events occurred every year (averaged using the complete years of 2012, 2015, and 2016). Fig. 13b shows the time series of the atmospheric pressure values associated with the nighttime heat wave events, exhibiting a high Corr. coef. of 0.96 with the nighttime heat wave events (Fig. 13a). The temperature range from these events was 4 to 20°C, with the most common temperatures between 10 and 12°C (Fig. 13c).A detailed examination of the days with lower air temperatures (4–7°C) demonstrated that during these days the diurnal temperature cycle was similar at 0°C and high atmospheric pressure (1020–1030 hPa) corresponded to the incursion of the southern edge of the Southeast Pacific Subtropical anti-cyclone (figure not shown). The monthly histogram of the nighttime heat wave events showed most occurrences in fall and winter, with fewer incidences in summer (Fig. 13d). Figure 14 presents an example of this event, which occurred during fall 2011, as shown in the atmospheric data from the oceanographic buoy installed in Puyuhuapi Fjord. The maximum SAT was observed on April 21, 2011, at midnight (00:00, local time), coinciding with a decreased atmospheric pressure, and increased surface wind intensity (Fig. 14a).

In order to explore the causes involved in the augmented air temperature, ERA5 reanalysis climate data sets were used (Fig. 14b–14g). Before the event, images from surface wind and atmospheric pressure showed the predominance of a westerly wind, from 45° - 56° S, and northerlies from 30°-35° S (Fig. 14b). At the same time, the SAT showed a meridional gradient, in which high air temperature covered the northern domain of the image (30°-40° S) (Fig. 14c). At midnight on July 21, 2011 (00:00, local time), an LAP system arrived in the eastern Austral Pacific Ocean water, and moved northward, interacting with the southern edge of an SPSA system. LAP systems rotate clockwise, with intense winds of ~25 m s^{-1}, and a minimum atmospheric pressure of 958 mbar (Fig. 14d). The west and northwest winds from the LAP advected southward the maximum air temperature, located north of 40° S, contributing to the increased air temperature and heat in Patagonia, as shown in Fig. 14a. High air temperature due to the LAP winds reached the southern part of Patagonia, close to the Magellan Strait (Fig. 14e). Atmospheric conditions returned to normal days after the LAP passage, (Fig. 14f and Fig. 14g) as shown in Fig. 14b and 14c.
A second example, using atmospheric data from the winter of 2012, demonstrated the increased SAT over Patagonia due to the LAP system influence better (Fig. 15). In this case, the maximum air temperature was again registered when the intensity of the wind increased and atmospheric pressure was low (Fig. 15a). Before this event, winds were from the north and northwest, but less intense, and the high air temperature presented the usual meridional gradient (Fig. 15b and Fig. 15c). At midnight of July 18, 2012, an LAP system entered the study area, and advected high air temperature from the subtropical area southward, to Patagonia. During this nighttime heat wave event, warm air was transported along the coast of Patagonia to ~56° S (Fig. 15d and Fig. 15e). Pre-event atmospheric conditions were restored one day after the passage of the LAP system (Fig. 15f and Fig. 15g).

4. **Discussion**

The combination of QuikSCAT, ASCAT and ERA5 surface wind products, together with in situ measurements of winds from oceanographic buoys and meteorological stations, has facilitated understanding of surface wind variability in the eastern Austral Pacific Ocean, and the Patagonian interior. Surface winds were generally westerlies (Fig. 2), and the synoptic scale dominated wind variability, due to the influence of the low/high atmospheric pressure systems, with winds from the northerly /southerly directions, respectively (Fig. 3-6). Implications of the synoptic scale events on the atmosphere-ocean interaction is the focus of this section of the manuscript, owing to the importance of winds to the oceanic responses, such as ET and EP, and their influence on the Patagonian climate.

4.1 Surface wind variability

Satellite data on the long term surface wind daily means, over the period 1999–2015, demonstrated that between 42° – 45° S, the normal wind was perpendicular to the coast, and blew from the west. From 45° S and to 56° S, the predominant wind direction changed to the northwest, reaching its highest intensity in the Magellan region, where it blew parallel to the coast. At the other end of the study region (40°–42° S), the predominant wind was from the southwest, although the intensity was less than in the Magellan region (Fig. 2). To date, the wind regime for this region has only been presented as a conceptual model, to show the influence of the westerlies on the westerly drift current (Thiel et al., 2007; Arkhipkin et al., 2009; Kilian and Lamy, 2012), and to present the general atmospheric circulation applicable to the west coast of South America (Rahn and Garreaud, 2013; Talley et al., 2011). Even though maps similar to Fig. 2 were presented in Aguirre et al., (2012) and Saldías et al., (2018), using QuikSCAT data, details of the surface wind behavior could not be determined. In addition, winds regime studies, which included derived variables such as EP and ET, focused on the central and northern region of the Chilean and Peruvian coasts, north of 40° S, and had as their main goals explanation of the dynamic of the Southeast Pacific Subtropical anti-cyclone (SPSA), and improved understanding of the wind's influence on this circulation regime (Ancapichun and Garcés-Vargas, 2015; Bravo et al., 2016; Fuenzalida et al., 2008; Schneider et al., 2017). Recently, the behavior and evolution of the ET in northern Patagonia was investigated along with its implications in the ocean response (Narváez et al., 2019). In the next section, these results will be incorporated and discussed.

LAP and HAP systems dominated mode 1 of the EOF, contributing ~30 % of the total variance (Fig. 3–6). In this mode, southerlies related to the passage of HAP systems, and northerlies produced by LAP systems (Fig. 7), occurred in a time scale of 16.5 days (Fig. 4–6 and Fig. 8). This illustrated the variability of surface winds in the eastern Austral Pacific Ocean, complementing the westerly winds which have been seen to dominate the wind regime, in average and seasonal data (Fig. 2).

EOF analysis detected wind from the west in mode 2 accounting for 22% of the total variance. This wind occurred mainly during spring-summer, before veering to an easterly wind for fall-winter (Fig. 3–6). A cycle change was observed in this mode using the individual QuikSCAT and ASCAT data sets and confirmed with the continuous data set of the ERA5 reanalysis (Fig. 8). During the first period an annual cycle dominated mode 2 (1999–2009), but in the second period (2009–2015), this dominance reduced, and cycle periods of 27.5 days and 16.5 days were observed (Fig. 8). The period of 16.5 days denoted the importance of the synoptic time scale, while the 27.5 day cycle suggested the influence of the recently reported Southern Hemisphere´s baroclinic annular mode (BAM), which has been described as displaying an energy band lasting between 20 and 30 days (Thompson and Barnes, 2014; Thompson and Woodworth, 2014). BAM influence was observed by Ross et al., (2015) in a Patagonian fjord (47.8° S), using Acoustic Doppler current profiler (ADCP) data, combined with in situ surface wind and atmospheric pressure records, highlighting the contribution of this atmospheric phenomenon to the intensification and frequency of the LAP systems that occur throughout the Patagonian. In addition, Narváez et al., (2019) reported the dominance of the BAM on an intraseasonal time scale showing an essential influence of this cycle in the atmospheric and oceanographic conditions of northern Patagonia (40°–45° S).

Finally, the EOF analysis allowed for the detection of the high surface wind variability in the eastern Austral Pacific Ocean, showing the dominance of the atmospheric pressure systems (e.g., LAP and HAP systems) over the various time scales. These atmospheric synoptic events occurred throughout the study region, coinciding with significant areas of the strongest westerly wind belt on earth (Chelton et al., 2004).

4.2 Atmospheric-ocean interactions

The long term ET mean showed that this movement ran parallel to the coast from between 40°and 48° S, and then from 48° S to 58° S, it ran perpendicular (onshore) to the coastline, showing higher magnitude in the Magellan region (Fig. 9). Studies have shown that when onshore ET occurred, downwelling conditions prevailed, and particulates were transported to the coast (Stewart, 2002), favoring the retention of eggs and larvae in the coastal zone (Epifanio and Garvine, 2001; Garland et al., 2002). It has also been shown that when offshore ET occurred, upwelling processes dominated along the coastline, favoring primary production (Escribano et al., 2016; Iriarte et al., 2012; Montero et al., 2007). As argued in the previous section, synoptic scale atmospheric events, such as LAP and HAP systems, dominated wind variability within the study area, especially in its northern domain, where the southern edge of the SPSA arrived during spring-summer. During this time of the year, northerly winds influenced the region, producing offshore ET, as shown by the ET time series for the northern (42.7° S) part of the study area (Fig. 10). Then, the upwelling process occurred along the coastline of Chiloe Island, as was demonstrated by the increased Chl-a and the drop of SST in the area of wind influence (Fig. 11). In addition, EP velocity was positively helping the upward movement of oceanic water, which enhanced the injection of nutrients into the surface layer (Rykaczewski and Checkley, 2008). Quantification of the Ekman downwelling/upwelling processes and their impact on the ocean response demonstrated the high contribution of the EP to the TUT in northern Patagonia (along with the west coast of Chiloé Island) over that of ET. These results imply that wind stress curl plays an essential role in the upward displacement of rich oceanic water to the surface layer. During the annual cycle, favorable upwelling conditions were observed from November to April (Figs. 10 and 11), the time of year with more intense photosynthetically available radiation (PAR) for phytoplankton species (Daneri et al., 2012).To date, coastal upwelling quantification using only the ET has been reported as south as the central coastal region of Chile (~36° S) (Sobarzo and Djurfeldt, 2004; Sobarzo et al., 2007) and recent analyses have been extended to 45° S (Narváez et al., 2019). However, our work has shown that coastal upwelling can also occur by EP and must be added to the TUT quantification for a realistic evaluation of the ocean response to surface wind. For example, in the California upwelling system, EP is more significant than ET for the TUT, especially during spring and summer (Pickett and Paduan, 2003). In northern Chile (27°–32° S) EP represented ~40% of the TUT, causing changes in the SST spatial structure (Bravo et al., 2016). Around Cabo Frío (22° S/ 42° W) EP was also the primary contributor process in the upwelling of the coldest water to the surface layer (Castelao and Barth, 2006).

From an inter-annual point of view, the TUT favored upwelling from spring 2015 to summer 2016, contributing to high Chl-a and FLH readings during summer 2016 (Fig. 11). A strong harmful algal bloom (HAB) was reported in northern Patagonia during February and March 2016, causing the death of 40.000 t of salmon (Díaz et al., 2019; Paredes et al., 2019). The main factors involved in the 2016 HAB included increased solar radiation, SST, and water column stratification, which were highlighted as trigger mechanisms (Léon-Muñoz et al., 2018). However, the results presented in this manuscript show that EP and ET favor the upwelling of nutrient-rich water to the euphotic layer, which can contribute to HAB development. Additionally, high ammonium concentration was observed two months later in the open oceanic water off the west coast of Chiloé Island (41° 46’ 15’’ S / 75° 43’ 31’’ W) due to the shedding to the sea of 4.600 t of dead salmon (Buschmann et al., 2016). As Fig. 11 shows, during this time EP favored the vertical ascent of water, inhibiting the sinking of the biochemical waste. Therefore, the Ekman upwelling process must be considered in the future for the decision makers during an environmental emergency.

In general, however, downwelling conditions, dominated by onshore ET, were observed in the study area, especially in the south, close to the Magellanic region (Fig. 9 and Fig. 10). We have hypothesized that the irregular orographic from 44° to 56° S, where the coast is conformed with many islands and channels, could reduce the possibility for oceanic water to sink at the coastline, allowing the opportunity for it to pass to the interior Patagonian fjords, carrying nutrients, eggs, larvae from many species into these areas, to enhance biological production in the southern Patagonian fjords.

In addition, it was noted that it was not only the ocean that responded to the synoptic scale variability of the surface wind, but that atmospheric conditions were also influenced. Two examples demonstrated the importance of synoptic scale events in modifying climate conditions in the Austral region (Fig. 14 and Fig. 15), where LAP systems contribute with the origin of the “Nighttime heat wave events.”

A conceptual model was built to explain the source of the nighttime heat wave events (Fig. 16). In this model, two atmospheric pressure systems participated: a permanent high pressure located in the north (SPSA), which transported warm air from the subtropical region (over the 40° S), and a synoptic LAP system, which originated in the south, with cold air from the Polar zone (Fig. 16a). The LAP originated in the Austral-Pacific Ocean, and the system moved northward, with intense winds rotating clockwise. The northward moving LAP stopped when it encountered the southern edge of the SPSA, at approximately 40° S (Fig. 16b). At this moment the stronger west and northwest wind from the LAP pulled in the warm air from the SPSA, and advected its heat southward to Patagonia. These events occur more frequently at nighttime, and their impact on the Patagonian climate depends on the intensity of the LAP system winds, and the heat content of the SPSA.

In the contexts of climate change and variability, any increase or trend of change in these events needs to be taken into account, as mechanisms that could contribute to increased glacial meltwater, and alteration of the Austral climate.

5. Conclusions

In our study, satellite and reanalysis wind data were used to understand surface wind variability in the eastern Austral Pacific Ocean, a region generally dominated by strong westerlies, and the SPSA. The EOF demonstrated that, within the area, mode 1, 2 and 3 of wind variability showed synoptic time scale dominance, due to the effects of low and high atmospheric pressure systems. Generally, downwelling conditions prevailed in the study region due to onshore ET, but offshore ET and upward EP were observed during spring and summer in the northern domain (~40° to 48° S), contributing to reduced SST, and Chl-a. The arrival of the southern edge of the SPSA during spring and summer created upwelling conditions dominated by EP, and this is the first time that this condition has been reported so far south. In addition, the SPSA was involved in generating the nighttime heat waves, acting with LAP systems to produce night time air temperature maxima which exceeded the normal midday maxima induced by solar radiation.

Data availability. All data sets used in this manuscript can be requested from the corresponding author.

Supplement. The supplement related to this article is available online.

Author contributions. IPS: designed the experiment, collection and analysis of the satellite data, and was the manuscript leader. RS: collection and analysis of the satellite and in situ data, as well as manuscript revision. WS: designed the experiment, collection and analysis of the satellite data, as well as manuscript revision. PL: data analysis of ERA5 and generation of Figure 1. DD: data analysis of ERA5 and validation process. EN: data analysis. CAC: validation process. GD: manuscript revision. All authors contributed to the writing this manuscript.

Competing interest. The authors declare that they have no conflict of interest.

Acknowledgments

Surface wind data was collected as part of FONDECYT Grants 3120038, and 11140161, by Dr. Iván Pérez-Santos, with assistance from Dr. Wolfgang Schneider's research group. Financial support was also provided by Centro Copas Sur Austral PFB31 and AFB170006. We are grateful to Centro Copas Sur Austral for providing data from its oceanographic buoy and a partial scholarship for Romanet Seguel to complete a Magister in Oceanography at the University of Concepción, Chile. We thank Centro de Investigación en Ecosistemas de la Patagonia (CIEP) for providing meteorological information. The ERA5 reanalysis data was provided by the Copernicus Climate Change Service (C3S) (2017): ERA5: Fifth generation of the ECMWF atmospheric reanalyses of the global climate. Copernicus Climate Change Service Climate Data Store (CDS). We appreciate the tremendous effort of the anonymous reviewers which led to improved manuscript quality.

References

Aguirre, C., Pizarro, Ó., Strub, P. T., Garreaud, R., & Barth, J. A.: Seasonal dynamics of the near-surface alongshore flow off central Chile. Journal of Geophysical Research: Oceans, 117(C1), n/a-n/a. https://doi.org/10.1029/2011JC007379, 2012.

Ancapichun, S. and Garcés-Vargas, J.: Variability of the Southeast Pacific Subtropical Anticyclone and its impact on sea surface temperature off north-central Chile. Ciencias Marinas, 41(1), 1–20. https://doi.org/10.7773/cm.v41i1.2338, 2015.

Arkhipkin, A. I., Schuchert, P. C., and Danyushevsky, L.: Otolith chemistry reveals fine population structure and close affinity to the Pacific and Atlantic oceanic spawning grounds in the migratory southern blue whiting (Micromesistiusaustralisaustralis). Fisheries Research, 96(2–3), 188–194. https://doi.org/10.1016/j.fishres.2008.11.002, 2009.

Bentamy, A., Croize-Fillon, D. and Perigaud, C.: Characterization of ASCAT measurements based on buoy and QuikSCAT wind vector observations Ocean Sci., 4, 265–274, 2008.

Bentamy A. and Croize-Fillon, D.: Gridded surface wind fields from Metop/ASCAT measurements. International Journal of Remote Sensing, 33, 1729-1754, 2011.

Bravo, L., Ramos, M., Astudillo, O., Dewitte, B., and Goubanova, K.: Seasonal variability of the Ekman transport and pumping in the upwelling system off central-northern Chile (~30° S) based on a high-resolution atmospheric regional model (WRF). Ocean Science, 12(5), 1049–1065. https://doi.org/10.5194/os-12-1049-2016, 2016.

Buschmann, A., Farías, L., Tapia, F., Varela, D., and Vásquez, M.: Informe Final: Comisión Marea Roja (CMR). Alphen aan den Rijn: Wolters Kluwer, 2016.

Castelao, R. M., and Barth J. A.: Upwelling around Cabo Frio, Brazil: The importance of wind stress curl, Geophys. Res. Lett., 33, L03602, doi:10.1029/2005GL025182, 2006.

Chelton, D.B., Schlax, M.G., Freilich, M.H., Milliff, R.F.: Satellite measurements reveal persistent small scale features in ocean winds. Science 303, 978e983, 2004.

Emery, W. J.and Thomson R. E.: Data analysis methods in physical oceanography, 634 pp, Pergamon Press, Oxford, 1998.

Epifanio, C. E. and Garvine, R. W.: Larval Transport on the Atlantic Continental Shelf of North America: a Review. Estuarine, Coastal and Shelf Science, 52, 51–77, doi:10.1006/ecss.2000.0727, 2001.

Escribano, R., Bustos-Ríos, E., Hidalgo, P., and Morales, C. E.: Non-limiting food conditions for growth and production of the copepod community in a highly productive upwelling zone. Continental Shelf Research, 126, 1–14.https://doi.org/10.1016/J.CSR.2016.07.018, 2016.

Fuenzalida, R., Schneider, W., Garcés-Vargas, J., and Bravo L.: Satellite altimetry data reveal jet-like dynamics of the Humboldt Current, J. Geophys. Res., 113, C07043, doi:10.1029/2007JC004684, 2008.

Garland, E. D., Zimmer, C.A., Lentz, S.J.: Larval Distributions in Inner-Shelf Waters: The Roles of Wind-Driven Cross-Shelf Currents and diel Vertical Migrations. Limnology and Oceanography, Vol. 47, No. 3, 803-817, 2002, Holton, J.: An Introduction to Dynamic Meteorology. Academic Press, San Diego, 511 pp, 1992.

Iriarte, J. L., Vargas, C. A., Tapia, F. J., Bermúdez, R., andUrrutia, R. E.: Primary production and plankton carbon biomass in a river-influenced upwelling area off Concepción, Chile. Progress in Oceanography, 92–95, 97–109. https://doi.org/10.1016/J.POCEAN.2011.07.009 2012.

Kaihatu, J.M., Handler, R.A., Marmorino, G.O., and Shay, L.K.: Empirical Orthogonal Function Analysis of Ocean Surface Currents Using Complex and Real-Vector Methods. J. Atmos. Oceanic Technol., 15, 927–941, doi: 10.1175/1520-0426(1998)015<0927:EOFAOO>2.0.CO;2, 1998.

Kamph, J. and Chapman, P.: Upwelling systems of the world: a scientific journey to the most productive marine ecosystems. Springer, Berlin, 425 pp, 2016.

Kilian, R.andLamy, F.: A review of Glacial and Holocene paleoclimate records from southernmost Patagonia (49–55°S). Quaternary Science Reviews, 53(C), 1–23. https://doi.org/10.1016/j.quascirev.2012.07.017, 2012.

Marcotte, D.:Cokrigeage with matlab, Computers and Geosciences, 17(9), 1265-1280, doi:10.1016/0098-3004(91)90028-C, 1991.

Montero, P., Daneri, G., Cuevas, L. A., González, H. E., Jacob, B., Lizárraga, L., and Menschel, E.: Productivity cycles in the coastal upwelling area off Concepción: The importance of diatoms and bacterioplankton in the organic carbon flux. Progress in Oceanography, 75(3), 518–530. https://doi.org/10.1016/j.pocean.2007.08.013, 2007.

Montero, P., Pérez-Santos, I., Daneri, G., Gutiérrez, M., Igor, G., Seguel, R., Crawford, D., and Duncan, P.: A winter dinoflagellate bloom drives high rates of primary production in a Patagonian fjord ecosystem, Estuar. Coast. ShelfSci., 199, 105-116, 2017.

Narváez, D., Vargas, C., Cuevas, A., García-Loyola, S., Lara, C., Segura, C., Tapia, F., Broitman, B.: Dominant scales of subtidal variability in coastal hydrography of the Northern Chilean Patagonia. Journal of Marine Systems, Volume 193, Pages 59-73, ISSN 0924-7963, https://doi.org/10.1016/j.jmarsys.2018.12.008, 2019.

Orlanski, I.: A rational subdivision of scales for atmospheric processes. Bulletin of the American Meteorological Society, 56: 527-530, 1975.Paredes, J., Varela D., Martínez C., Zúñiga A., Correa K., Villarroel A. and Olivares B.: Population Genetic Structure at the Northern Edge of the Distribution of Alexandrium catenella in the Patagonian Fjords and Its Expansion Along the Open Pacific Ocean Coast. Front. Mar. Sci. 5:532.doi: 10.3389/fmars.2018.00532, 2019.

Pérez-Santos, I., Schneider, W., Sobarzo, M., Montoya-Sánchez, R., Valle-Levinson, A., and Garcés-Vargas, J.: Surface wind variability and its implications for the Yucatan basin-Caribbean Sea dynamics. Journal of Geophysical Research, 115 (C10), C10052. https://doi.org/10.1029/2010JC006292, 2010.

Pickett, M. H. and Paduan J. D.: Ekman transport and pumping in the California Current based on the U.S. Navy's high resolution atmospheric model (COAMPS), J. Geophys. Res., 108(C10), 3327, doi:10.1029/2003JC001902, 2003.

Piolle, J. F. and Bentamy, A.: Mean Wind Fields (MWF product), User Manual, QuikSCAT, CERSAT, Plouzané, 42pp, 2002.

Rahn, D. and Garreaud, R.: A synoptic climatology of the near-surface wind along the west coast of South America. Int. J. Climatol.1-13, 2013.

Ray, P.S.: Mesoscale Meteorology and Forecasting. American Meteorological Society, Boston, MA, 793 pp, 1986.

Ross, L., Valle-Levinson, A., Pérez-Santos, I., Tapia, F.,and Schneider, W.: Baroclinic annular variability of internal motions in a Patagonian fjord. Journal of Geophysical Research: Oceans, 120, 5668– 5685. https://doi.org/10.1002/2015JC011264, 2015.

Rykaczewski, R. R. and Checkley, D.M.: Influence of ocean winds on the pelagic ecosystem in upwelling regions. PNAS, 105-6, 1965–1970, 2008.

Saldías, G.S., Sobarzo, M., and Quiñones, R.: Freshwater structure and its seasonal variability off western Patagonia. Progress in Oceanography, https://doi.org/10.1016/j.pocean.2018.10.014, 2018.

Schneider, W., Donoso, D., Garcés-Vargas, J., and Escribano, R.: Water-column cooling and sea surface salinity increase in the upwelling region off central-south Chile driven by a poleward displacement of the South Pacific High. Progress in Oceanography, 151, 38–48. https://doi.org/10.1016/j.pocean.2016.11.004, 2017.

Smith, R. L.: Upwelling, Oceanogr, Mar. Biol. Annu. Rev. 6,11-46, 1968.

Sobarzo, M. and Djurfeldt, L.: Coastal upwelling process on a continental shelf limited by submarine canyons, Concepción, central Chile, J. Geophys. Res., 109, C12012, doi:10.1029/2004JC002350, 2004.

Sobarzo, M., Bravo, L., Donoso, D., Garcés-Vargas, J., and Schneider, W.: Coastal upwelling and seasonal cycles that influence the water column over the continental shelf off central Chile, Progress in Oceanography 75, 363–382, 2007.

Stewart, R. H.: Introduction to physical oceanography, Spring 2002 Edition, Department of Oceanography, Texas A and M University, 350pp, 2002.

Talley, L.D., Pickard, G.L., Emery, W.J., and Swift, J.H.: Descriptive physical oceanography, an introduction. Six edition, Academic press, Elsevier, 1-983, 2011.

Taylor, K. E.: Summarizing multiple aspects of model performance in a single diagram, J. Geophys. Res., 106, 7183–7192, doi:10.1029/592 2000JD900719, 2001.

Thiel, M. et al.: The Humboldt Current system of northern and central Chile. Oceanography and Marine Biology: An Annual Review, 45, 195-344 © R. N. Gibson, R. J. A. Atkinson, and J. D. M. Gordon, Editors Taylor and Francis, 2007.

Thompson, D. W. J. and Barnes, E. A.: Periodic variability in the large-scale southern hemisphere atmospheric circulation, Science, 343, 641–645, 2014.

Thompson, D. W. J.and Woodworth J. D.: Barotropic and baroclinic annular variability in the southern hemisphere, J. Atmos. Sci., 71, 1480–1493, doi:10.1175/JAS-D-13-0185.1, 2014.

Thurman, H.V. and Trujillo, A.P.: Introductory Oceanography. Tenth edition, Pearson, Prentice Hall, Upper Saddle River, New Jersey 07458, 597pp, 2004.

Tomasz, N.: Chapter Two - El Niño/Southern Oscillation and Selected Environmental Consequences, Advances in Geophysics, Elsevier, Volume 55, Pp 77-122, 2014.

Tomczak, M. and Godfrey, J. S.: Regional Oceanography: An Introduction, 422 pp, Pergamon, 1994.

Torrence, C.and Compo, G. P.: A Practical Guide to Wavelet Analysis, Bull. Amer. Meteor. Soc., 79, 61–78, doi: 10.1175/1520-0477(1998)079<0061:APGTWA>2.0.CO;2, 1998.

Yelland, M.and Taylor, P.K.: Wind Stress Measurements from the Open Ocean, J. Phys. Oceanogr., 26, 541–558, doi: 10.1175/1520-0485(1996)026<0541:WSMFTO>2.0.CO; 2, 1996.

Figure captions

Figure 1. Map of the study area and geographical position of the sampling stations. Bathymetric image of the seafloor and topography obtained from https://www.gmrt.org/GMRTMapTool.

Figure 2. Long term mean of daily surface wind from (**a**) QuikSCAT (1999–2009), (**b**) ASCAT (2007–2016) and (**c**) ERA5 reanalysis climate data sets (1999–2015). Black line: standard deviations of daily data. Colored bar: surface wind magnitude.

Figure 3. Eastern Austral Pacific Ocean, 1999 to 2015: normalized eigenvector patterns, from QuikSCAT (**a**, **b**) and (**c**), ASCAT (**d**, **e**, and **f**) and ERA5 reanalysis (**g**, **h** and **i**).

Figure 4. (**a**, **d**, and **g**) Normalized time series of the time-dependent coefficient (black lines) from the 30 day, low pass filtered time series (solid red lines). (**b**, **e**, and **h**) Global wavelet spectra (black solid lines) with 95% confidence interval (red dashed lines), and (**c**, **f**, and **i**) long term monthly mean of EOF modes from surface winds daily data on QuikSCAT from 1999 to 2009: mode 1 (**a**, **b**, and **c**), mode 2 (**d**, **e**, and **f**), mode 3 (**g**, **h**, and **i**).

Figure 5. (**a**, **d**, and **g**) Normalized time series of the time-dependent coefficient (black lines) from the 30 day, low pass filtered time series (solid red lines). (**b**, **e**, and **h**) Global wavelet spectra (black solid lines) with 95% confidence interval (red dashed lines) and (**c**, **f**, and **i**) long term, monthly mean of EOF modes from surface winds daily data on ASCAT from 2007 to 2015: mode 1 (**a**, **b**, and **c**), mode 2 (**d**, **e**, and **f**), mode 3 (**g**, **h**, and **i**).

Figure 6. (**a**, **d**, and **g**) Normalized time series of the time-dependent coefficient (black lines) from the 30 day, low pass filtered time series (solid red lines). (**b**, **e**, and **h**) Global wavelet spectra (black solid lines) with 95% confidence interval (red dashed lines), and (**c**, **f**, and **i**) long term monthly mean of EOF modes from surface winds daily data of ERA5 reanalysis from 1999 to 2015: mode 1 (**a**, **b**, and **c**), mode 2 (**d**, **e**, and **f**), mode 3 (**g**, **h**, and **i**).

Figure 7. Snapshots of the surface winds representing EOF eigenvector spatial structures for mode 1 (**a** and **b**), mode 2 (**c** and **d**); and mode 3 (**e** and **f**). Surface wind and atmospheric pressure data were obtained from the ERA5 reanalysis climate product. The surface wind vectors were plotted with a spatial resolution of 1°×1°. The red rectangle in (**a**) indicates the study area.

Figure 8. Morlet wavelet power spectrum applied to the three series of the EOF time-dependent coefficient from QuikSCAT (**a**, **c**, and **e**), from ASCAT (**b**, **d**, and **f**) and from the ERA5 (**g**, **h**, and **i**).The fine contour lines enclose regions of confidence levels of >95% for a red noise process with a lag 1 coefficient between 0.52 and 0.55, and the thick contour lines indicate the cone of influence. The color bar relates colors on the power spectrum.

Figure 9. Long term mean of daily ET (red arrows), and EP (color bars) from (**a**) QuikSCAT (1999–2009), (**b**) ASCAT (2007–2016) and (**c**) ERA5 reanalysis (1999–2015). The black lines represent the zero value of EP, where a positive number is a region favorable to upwelling and negative to downwelling.

Figure 10. Quantification of the cross-shore transport using ERA5 reanalysis from the north, center and south time series (see Fig. 1 for the position) from 1999-–2018. (**a**, **d**, and **g**) represent the long term daily mean, (**b**, **e**, and **h**) the long term monthly mean, and (**c**, **f**, and **i**) cumulative ET, EP, and TUT. The TUT is the sum of the ET and EP. The positive/negative values of transport indicate upwelling/downwelling conditions.

Figure 11. Time series of (**a**) the TUT from ERA5, (**b**) the Chl-a anomalies, (**c**) the FLH anomalies and (**d**) the SST anomalies from the MODIS-Aqua satellite data. (**e**-**h**) Examples showing the ocean response to ET and EP along the northern coast of Patagonia. SST (**e** and **g**), and Chl-a (**f** and **h**) from MODIS-Aqua.

Figure 12. SAT and net solar radiation long term hourly means with histogram of the maximum SAT and spectral analysis, from the Puyuhuapi Fjord oceanographic buoy (**a**, **b**, **c**, and **g**), and meteorological station (**d**, **e**, **f**, and **h**), for 2011−2017. The gray shaded area in (**e** and **f**) shows the times of the second air temperature maxima. The error bars in (**a**, **b**, **d** and **e**) represent the standard deviations of each variable.

Figure 13. (**a**) Time series of the nighttime heat wave events (**b**) atmospheric pressure during the events, (**c**) related histogram, and (**d**) long term monthly mean from 2011 to 2017. Data were obtained from the Puyuhuapi Fjord oceanographic buoy (2011–2013) and meteorological station (2014–2017).From July 2013 to April 2014 no data was collected. The red circle in (**a** and **b**) denotes the position of the nighttime heat wave events described in Figs. 14 and 15.

Figure 14. Hourly air temperature, atmospheric pressure, and wind speed data from the Puyuhuapi Fjord oceanographic buoy (**a**) and surface winds, atmospheric pressure and surface air temperature from the ERA5 reanalysis climate product (**b** – **g**), during April 2011. The surface wind vectors (**b**, **d**, and **f**) were plotted with a spatial resolution of 1°×1°.

Figure 15. Hourly air temperature, atmospheric pressure, and wind speed data from the Puyuhuapi Fjord oceanographic buoy (a) and surface winds, atmospheric pressure and surface air temperature from ERA5 reanalysis climate product (**b** – **g**), during July 2012. The surface wind vectors (**b**, **d**, and **f**) were plotted with a spatial resolution of 1°×1°.

Figure 16. A conceptual model of the “Night-time heat wave event” in the Eastern Austral Pacific Ocean. (**a**) The initial condition, where a low atmospheric pressure system with cold air and a high atmospheric pressure system with warm air are regionally present, although separate; (**b**) the low atmospheric pressure system moves northward and encounters the high atmospheric pressure system, advecting warm air to Patagonia.

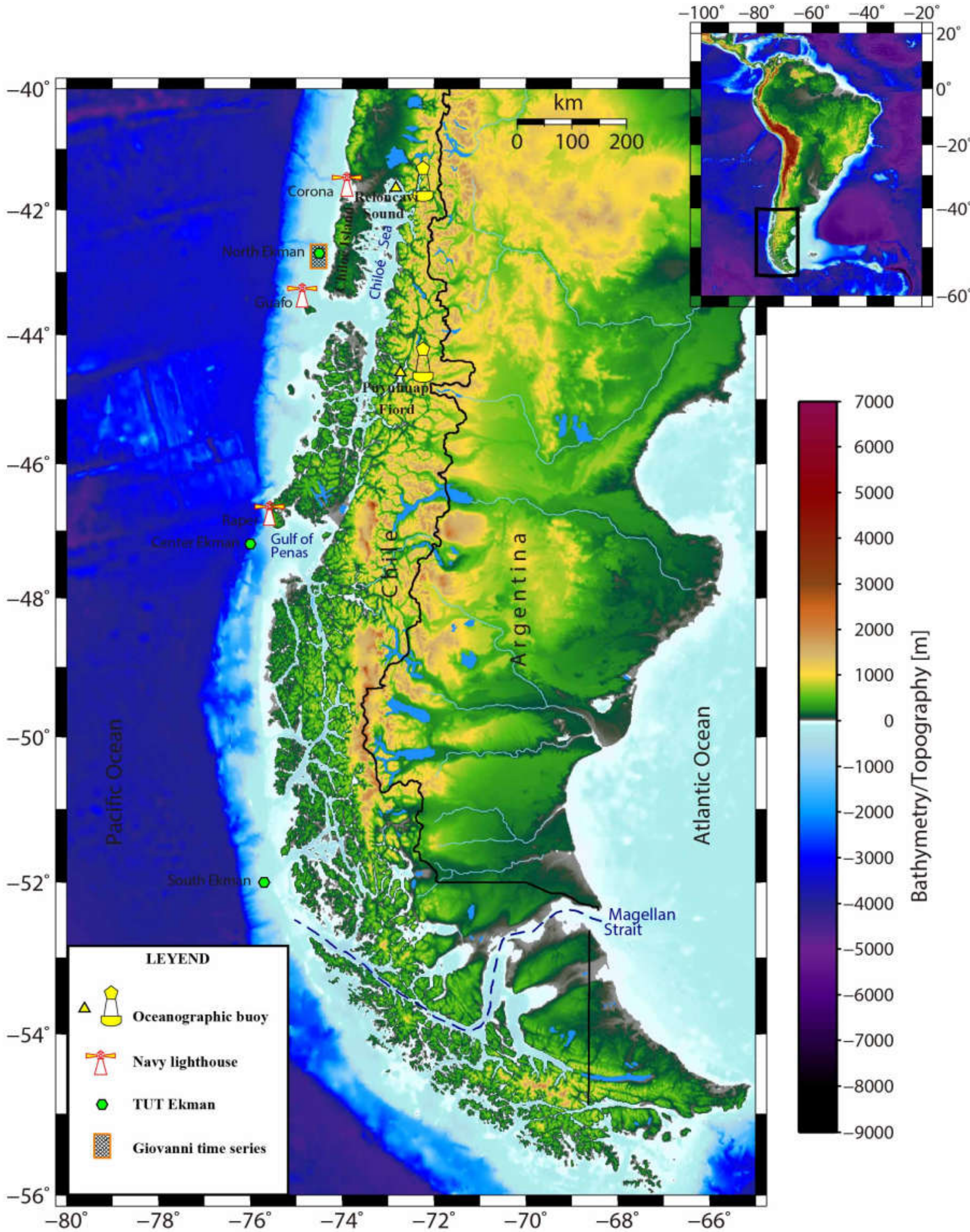

Figure 1. Map of the study area and geographical position of the sampling stations. Bathymetric image of the seafloor and topography obtained from https://www.gmrt.org/GMRTMapTool.

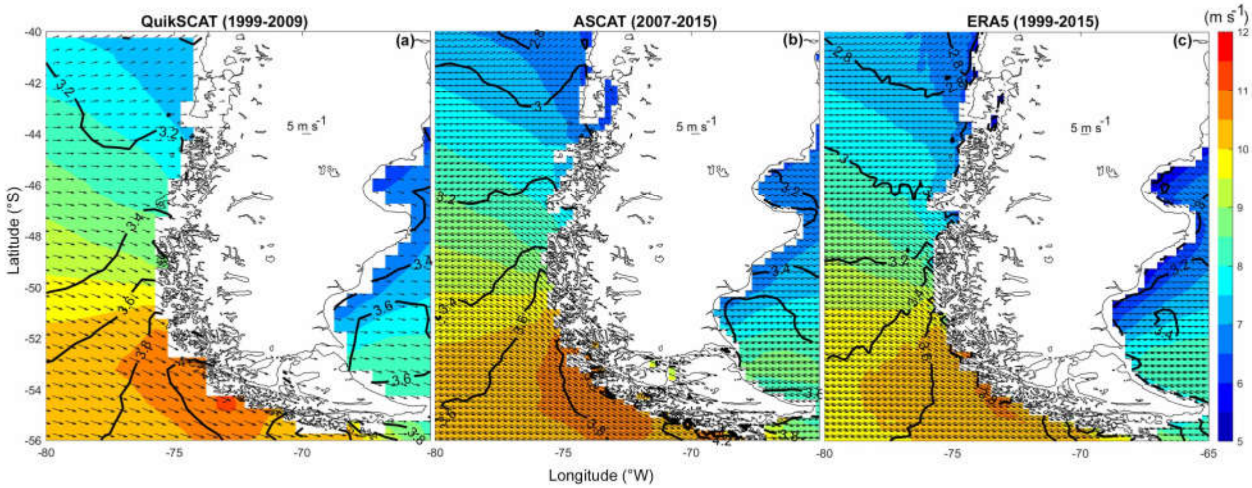

Figure 2. Long term mean of daily surface wind from (**a**) QuikSCAT (1999–2009), (**b**) ASCAT (2007–2016) and (**c**) ERA5 reanalysis climate data sets (1999–2015). Black line: standard deviations of daily data. Colored bar: surface wind magnitude.

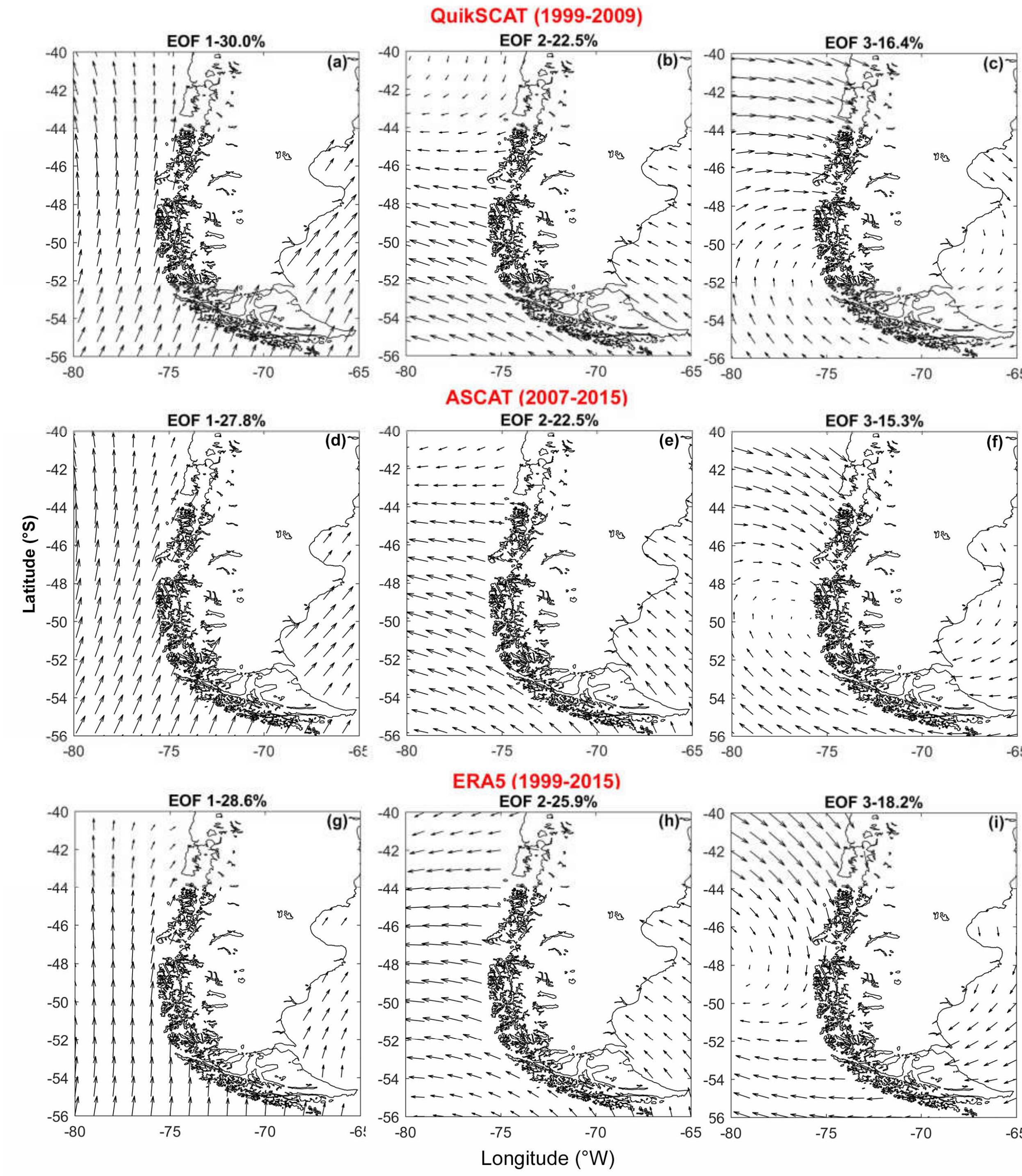

700 Figure 3. Eastern Austral Pacific Ocean, 1999 to 2015: normalized eigenvector patterns, from QuikSCAT (**a**, **b**) and (**c**), ASCAT (**d**, **e**, and **f**) and ERA5 reanalysis (**g**, **h** and **i**).

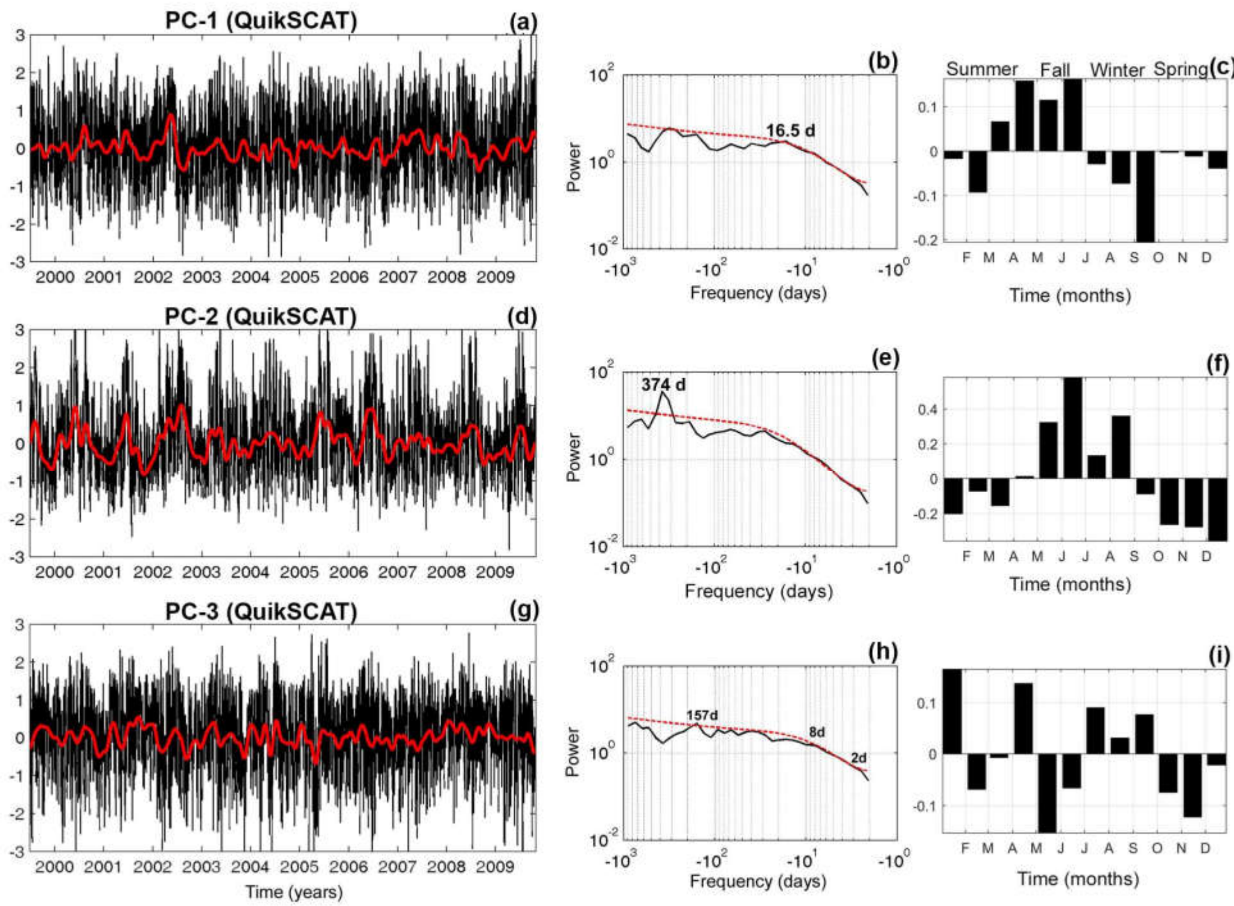

Figure 4. (**a**, **d**, and **g**) Normalized time series of the time-dependent coefficient (black lines) from the 30 day, low pass filtered time series (solid red lines). (**b**, **e**, and **h**) Global wavelet spectra (black solid lines) with 95% confidence interval (red dashed lines), and (**c**, **f**, and **i**) long term monthly mean of EOF modes from surface winds daily data on QuikSCAT from 1999 to 2009: mode 1 (**a**, **b**, and **c**), mode 2 (**d**, **e**, and **f**), mode 3 (**g**, **h**, and **i**).

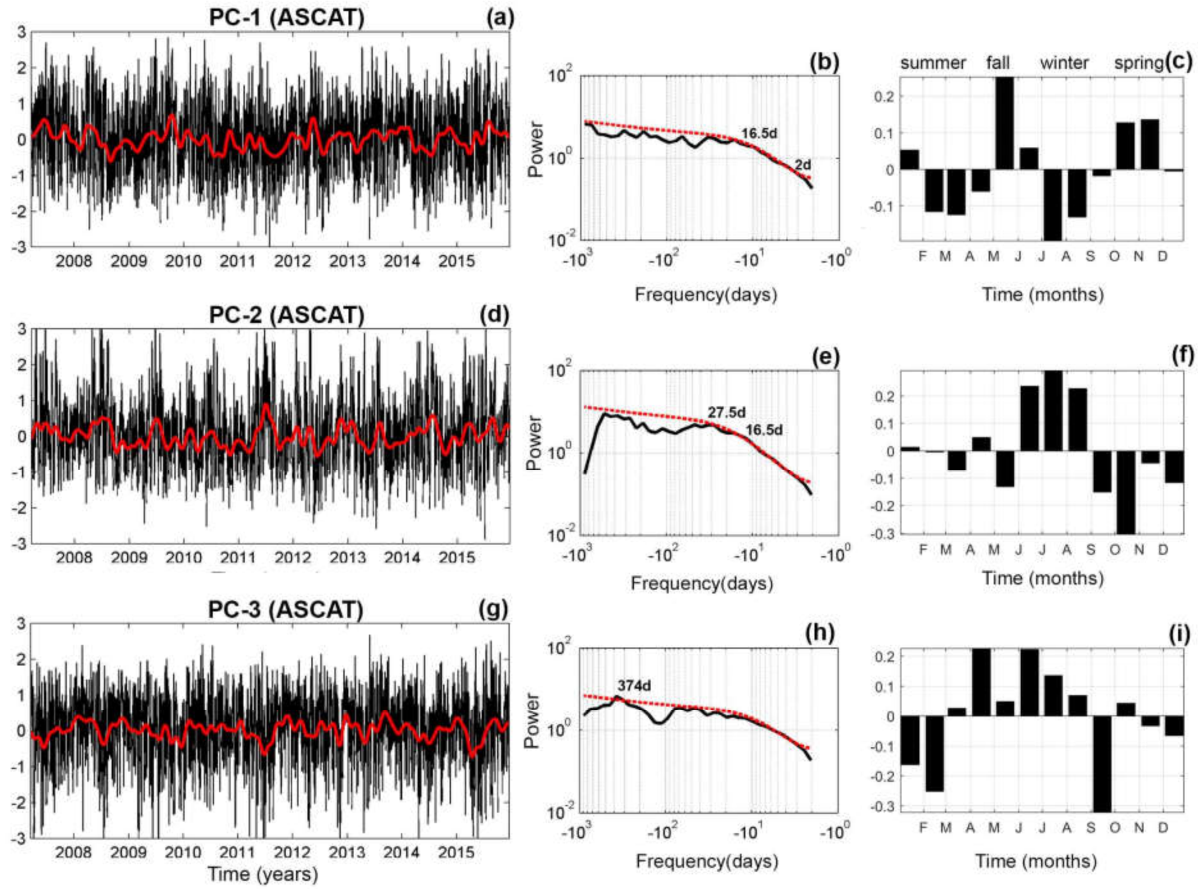

Figure 5. (**a**, **d**, and **g**) Normalized time series of the time-dependent coefficient (black lines) from the 30 day, low pass filtered time series (solid red lines). (**b**, **e**, and **h**) Global wavelet spectra (black solid lines) with 95% confidence interval (red dashed lines) and (**c**, **f**, and **i**) long term, monthly mean of EOF modes from surface winds daily data on ASCAT from 2007 to 2015: mode 1 (**a**, **b**, and **c**), mode 2 (**d**, **e**, and **f**), mode 3 (**g**, **h**, and **i**).

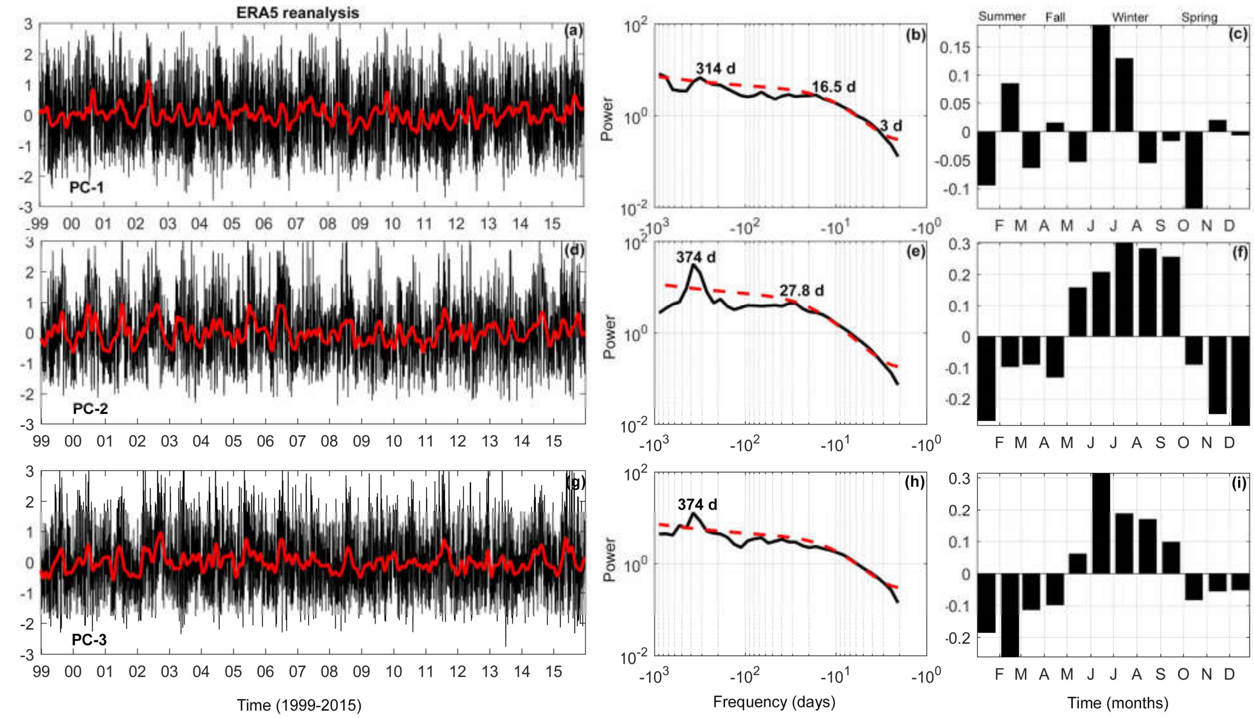

Figure 6. (**a**, **d**, and **g**) Normalized time series of the time-dependent coefficient (black lines) from the 30 day, low pass filtered time series (solid red lines). (**b**, **e**, and **h**) Global wavelet spectra (black solid lines) with 95% confidence interval (red dashed lines), and (**c**, **f**, and **i**) long term monthly mean of EOF modes from surface winds daily data of ERA5 reanalysis from 1999 to 2015: mode 1 (**a**, **b**, and **c**), mode 2 (**d**, **e**, and **f**), mode 3 (**g**, **h**, and **i**).

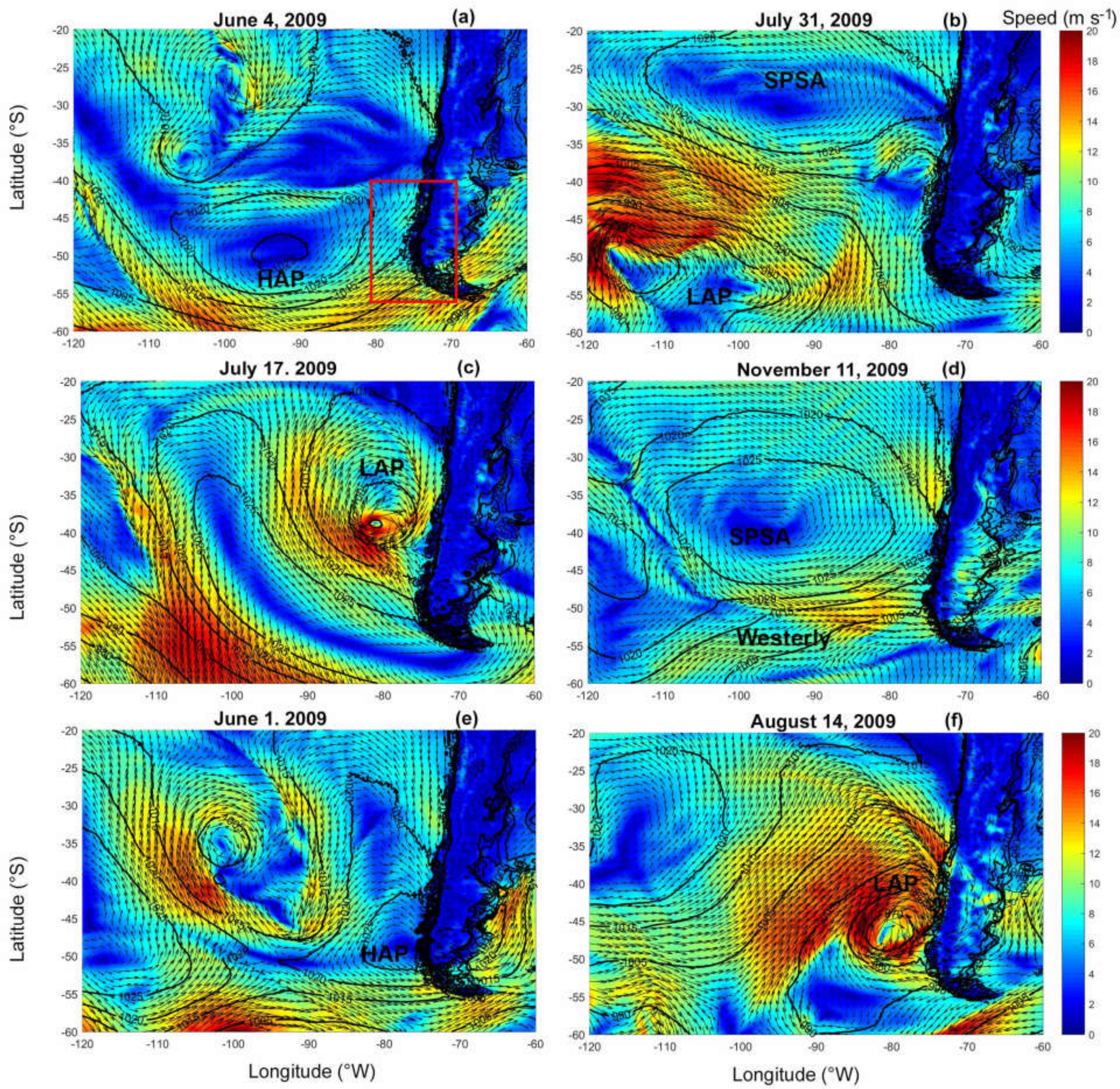

Figure 7. Snapshots of the surface winds representing EOF eigenvector spatial structures for mode 1 (**a** and **b**), mode 2 (**c** and **d**); and mode 3 (**e** and **f**). Surface wind and atmospheric pressure data were obtained from the ERA5 reanalysis climate product. The surface wind vectors were plotted with a spatial resolution of 1°×1°. The red rectangle in (**a**) indicates the study area.

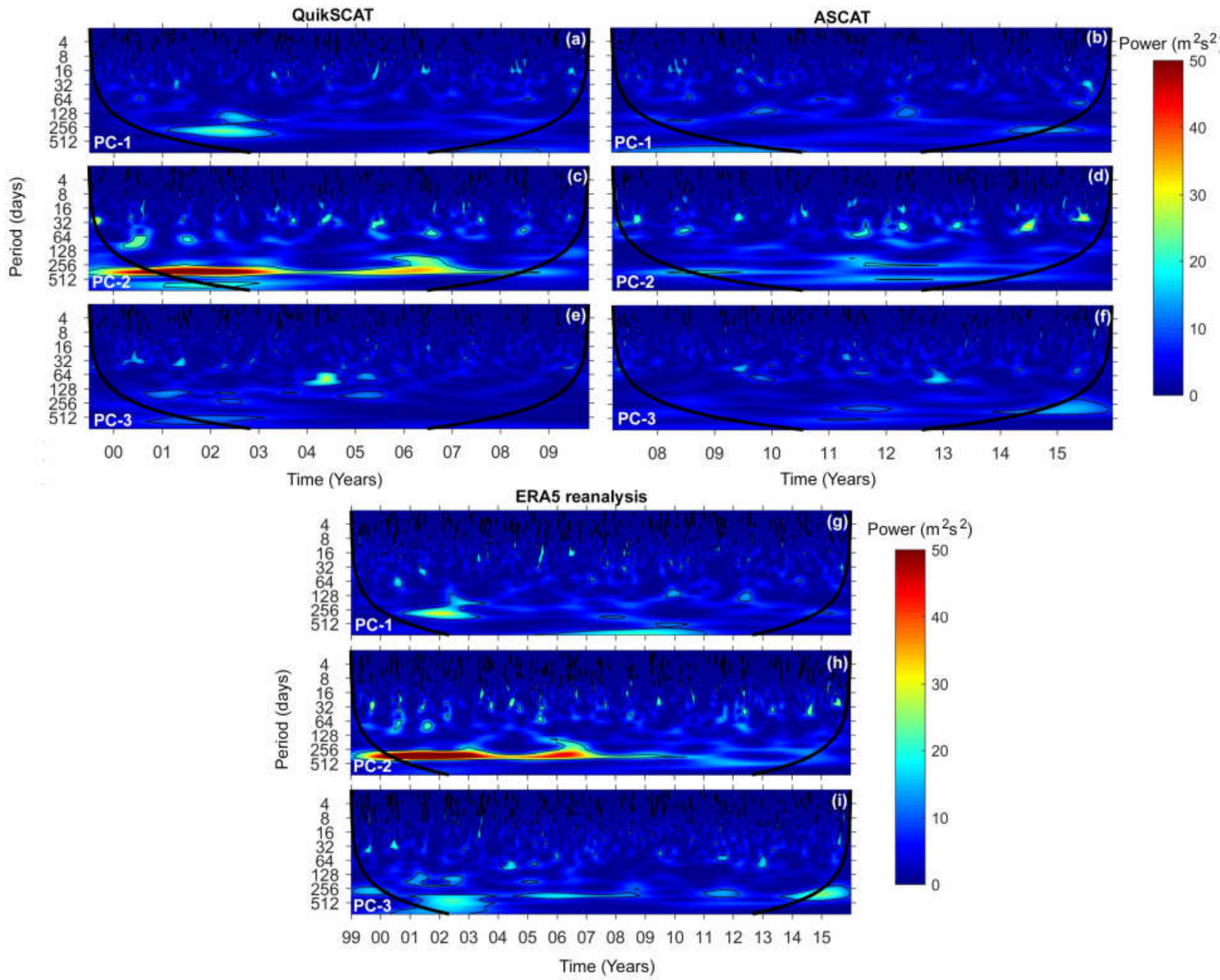

740 Figure 8. Morlet wavelet power spectrum applied to the three series of the EOF time-dependent coefficient from QuikSCAT (**a**, **c**, and **e**), from ASCAT (**b**, **d**, and **f**) and from the ERA5 (**g**, **h**, and **i**).The fine contour lines enclose regions of confidence levels of >95% for a red noise process with a lag 1 coefficient between 0.52 and 0.55, and the thick contour lines indicate the cone of influence. The color bar relates colors on the power spectrum.

745

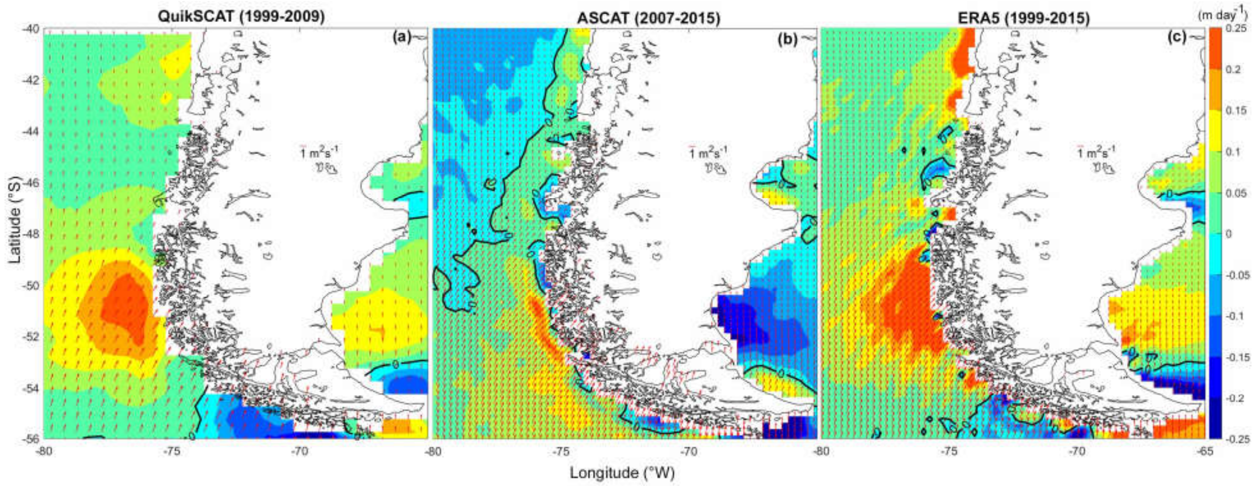

Figure 9. Long term mean of daily ET (red arrows), and EP (color bars) from (**a**) QuikSCAT (1999–2009), (**b**) ASCAT (2007–2016) and (**c**) ERA5 reanalysis (1999–2015). The black lines represent the zero value of EP, where a positive number is a region favorable to upwelling and negative to downwelling.

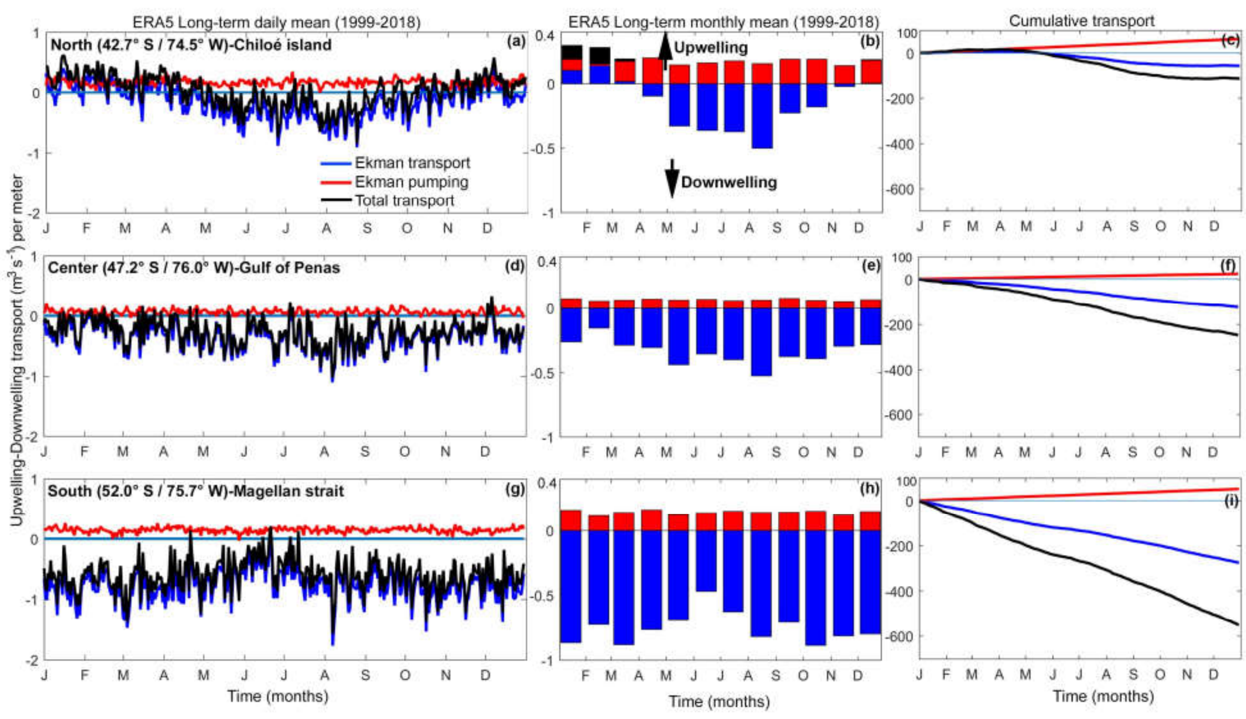

Figure 10. Quantification of the cross-shore transport using ERA5 reanalysis from the north, center and south time series (see Fig. 1 for the position) from 1999–2018. (**a**, **d**, and **g**) represent the long term daily mean, (**b**, **e**, and **h**) the long term monthly mean, and (**c**, **f**, and **i**) cumulative ET, EP, and TUT. The TUT is the sum of the ET and EP. The positive/negative values of transport indicate upwelling/downwelling conditions.

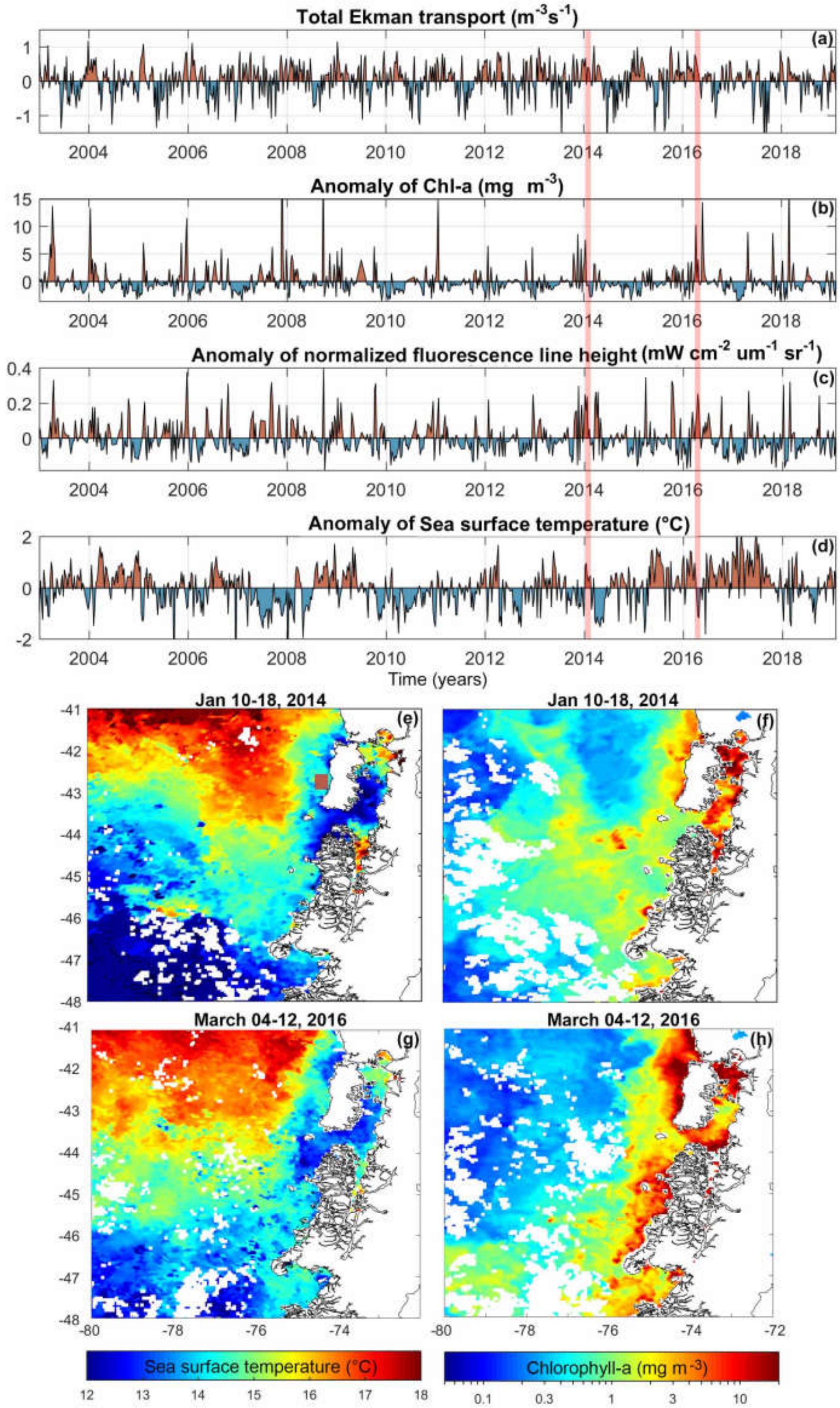

Figure 11. Time series of (**a**) the TUT from ERA5, (**b**) the Chl-a anomalies, (**c**) the FLH anomalies and (**d**) the SST anomalies from the MODIS-Aqua satellite data. (**e**-**h**) Examples showing the ocean response to ET and EP along the northern coast of Patagonia. SST (**e** and **g**), and Chl-a (**f** and **h**) from MODIS-Aqua.

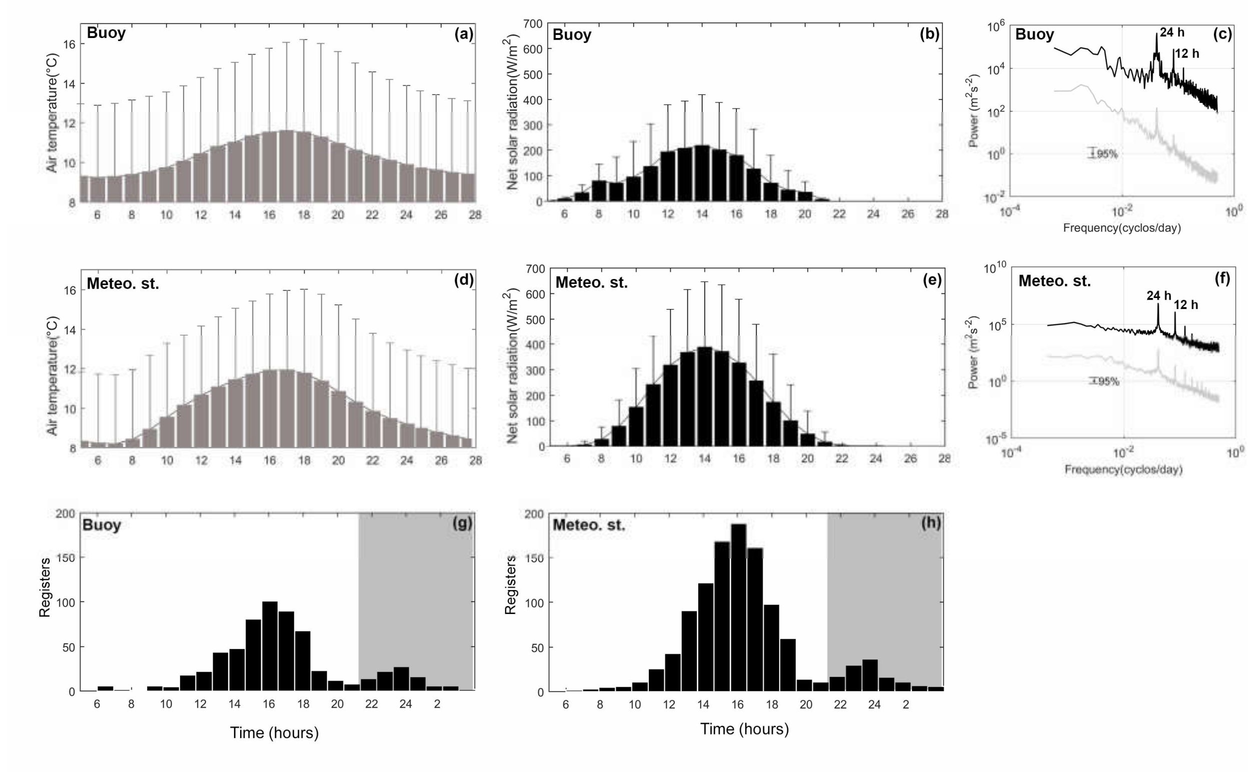

Figure 12. SAT and net solar radiation long term hourly means with histogram of the maximum SAT and spectral analysis, from the Puyuhuapi Fjord oceanographic buoy (**a**, **b**, **c**, and **g**), and meteorological station (**d**, **e**, **f**, and **h**), for 2011−2017. The gray shaded area in (**e** and **f**) shows the times of the second air temperature maxima. The error bars in (**a**, **b**, **d** and **e**) represent the standard deviations of each variable.

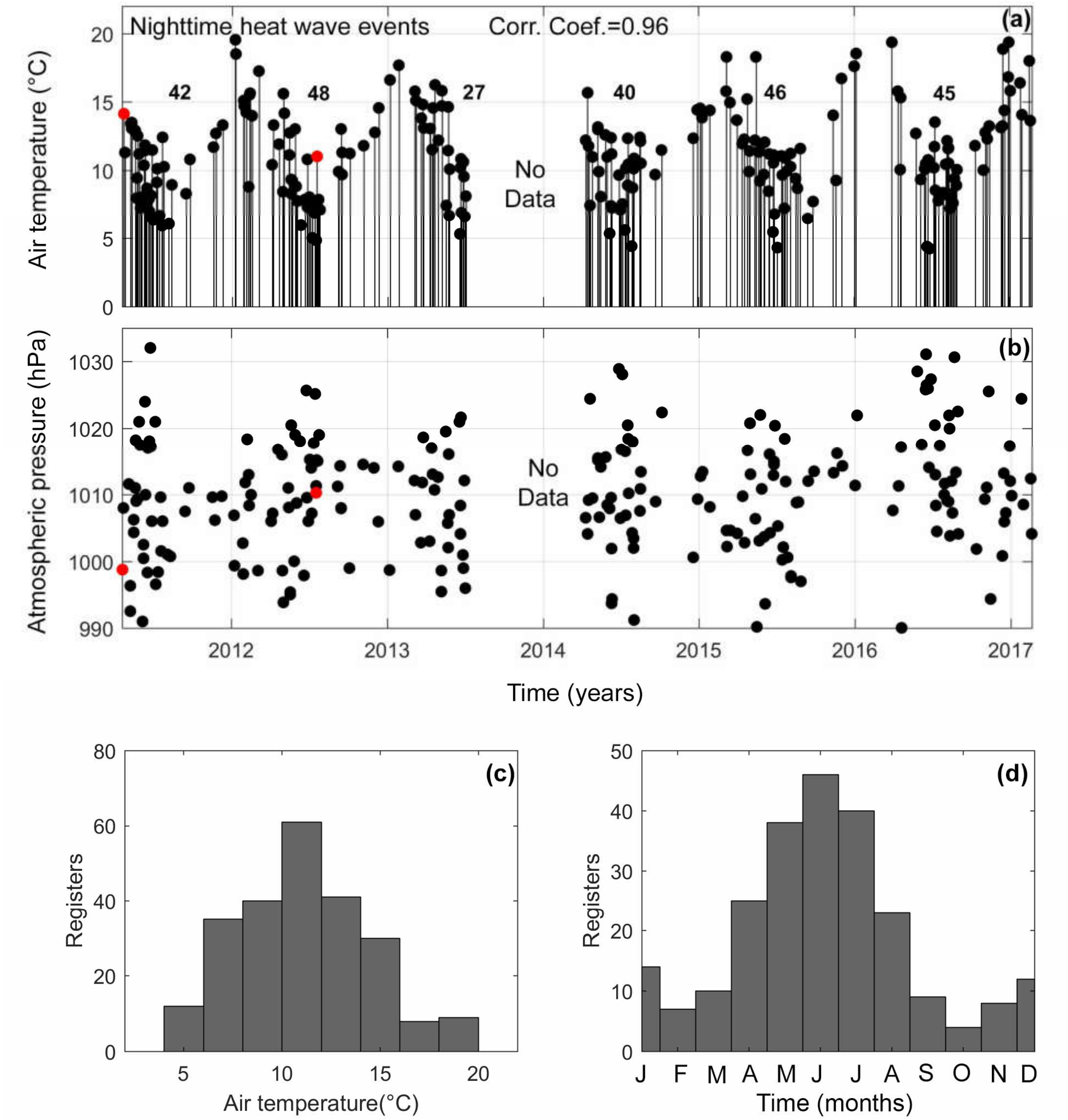

Figure 13. (**a**) Time series of the nighttime heat wave events (**b**) atmospheric pressure during the events, (**c**) related histogram, and (**d**) long term monthly mean from 2011 to 2017. Data were obtained from the Puyuhuapi Fjord oceanographic buoy (2011–2013) and meteorological station (2014–2017).From July 2013 to April 2014 no data was collected. The red circle in (**a** and **b**) denotes the position of the nighttime heat wave events described in Figs. 14 and 15.

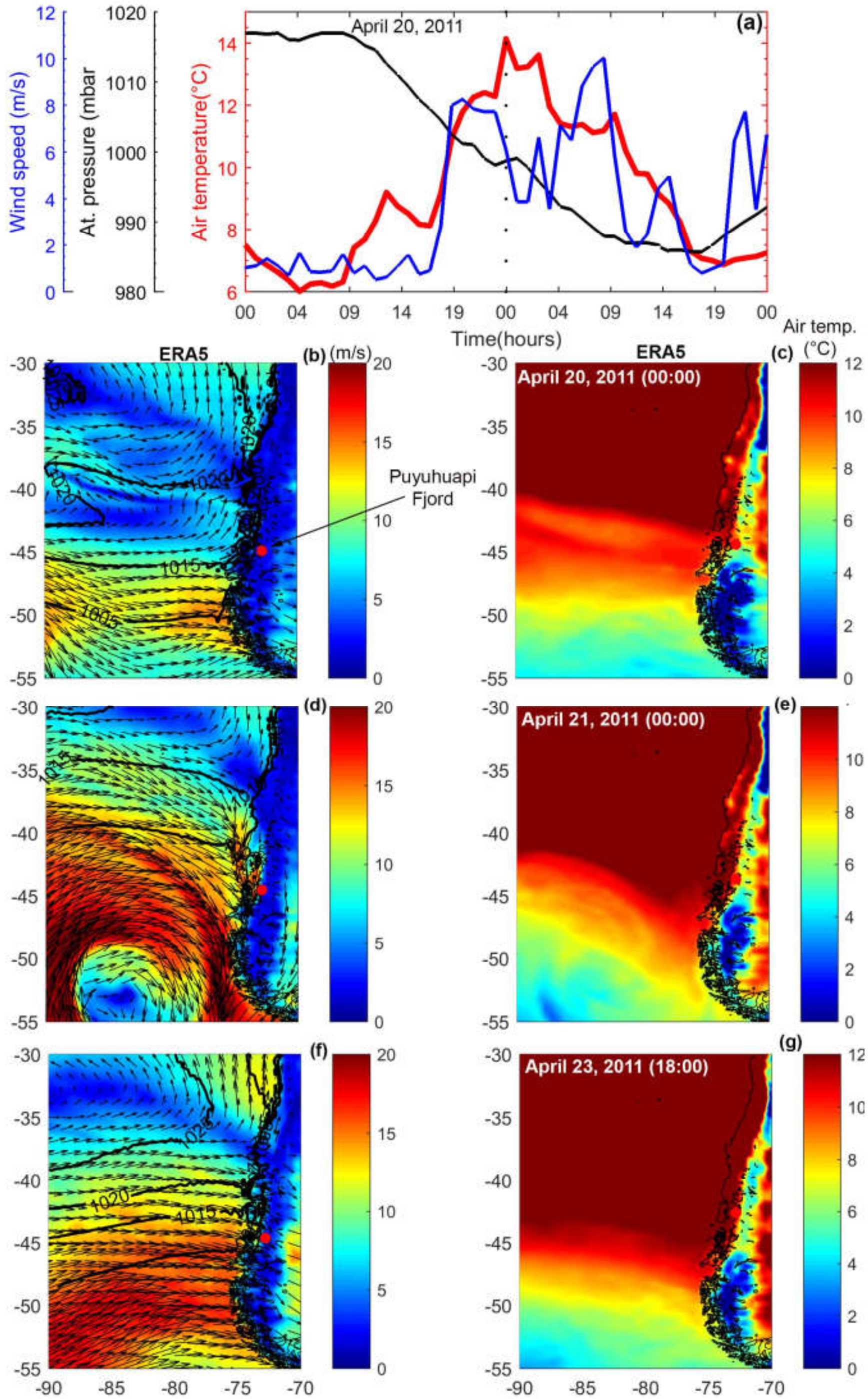

Figure 14. Hourly air temperature, atmospheric pressure, and wind speed data from the Puyuhuapi Fjord
780 oceanographic buoy (**a**) and surface winds, atmospheric pressure and surface air temperature from the ERA5 reanalysis climate product (**b** – **g**), during April 2011. The surface wind vectors (**b**, **d**, and **f**) were plotted with a spatial resolution of 1°×1°.

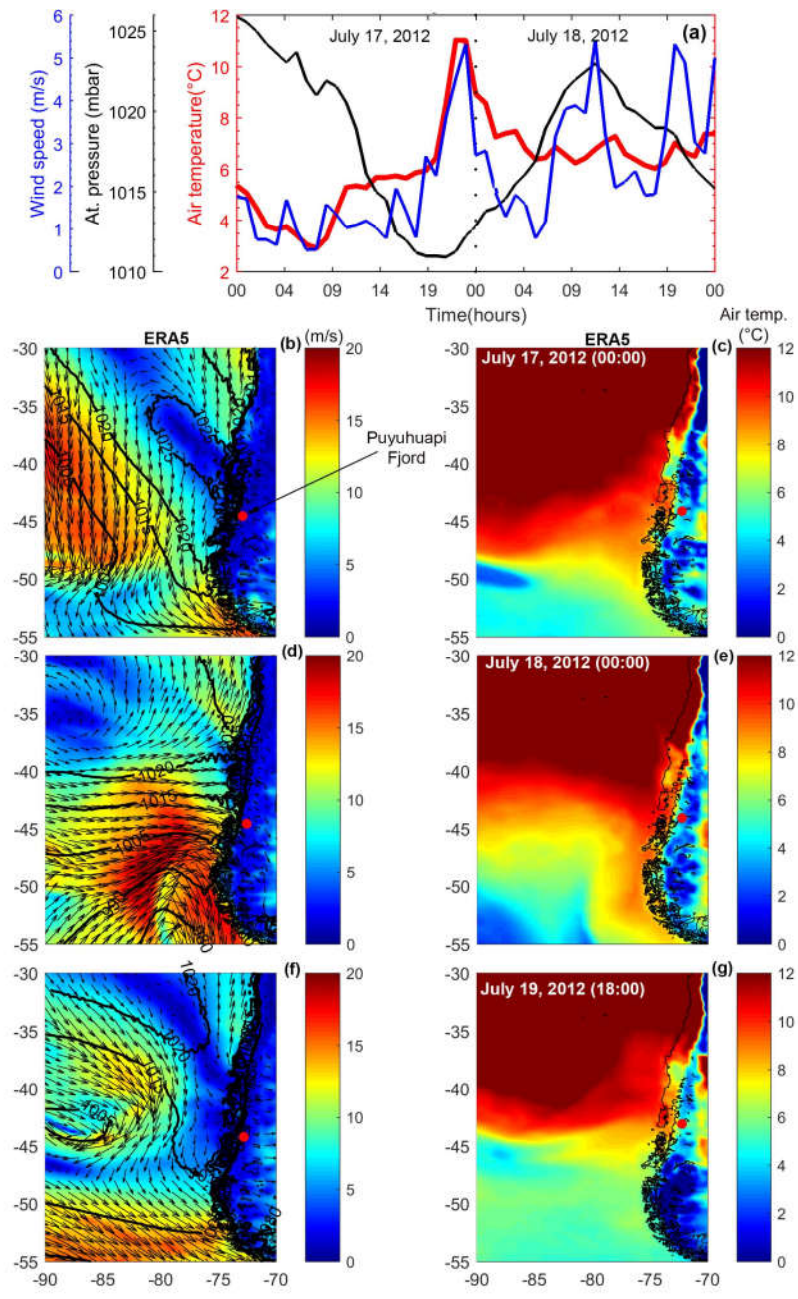

Figure 15. Hourly air temperature, atmospheric pressure, and wind speed data from the Puyuhuapi Fjord oceanographic buoy (a) and surface winds, atmospheric pressure and surface air temperature from ERA5 reanalysis climate product (**b**–**g**), during July 2012. The surface wind vectors (**b**, **d**, and **f**) were plotted with a spatial resolution of 1°×1°.

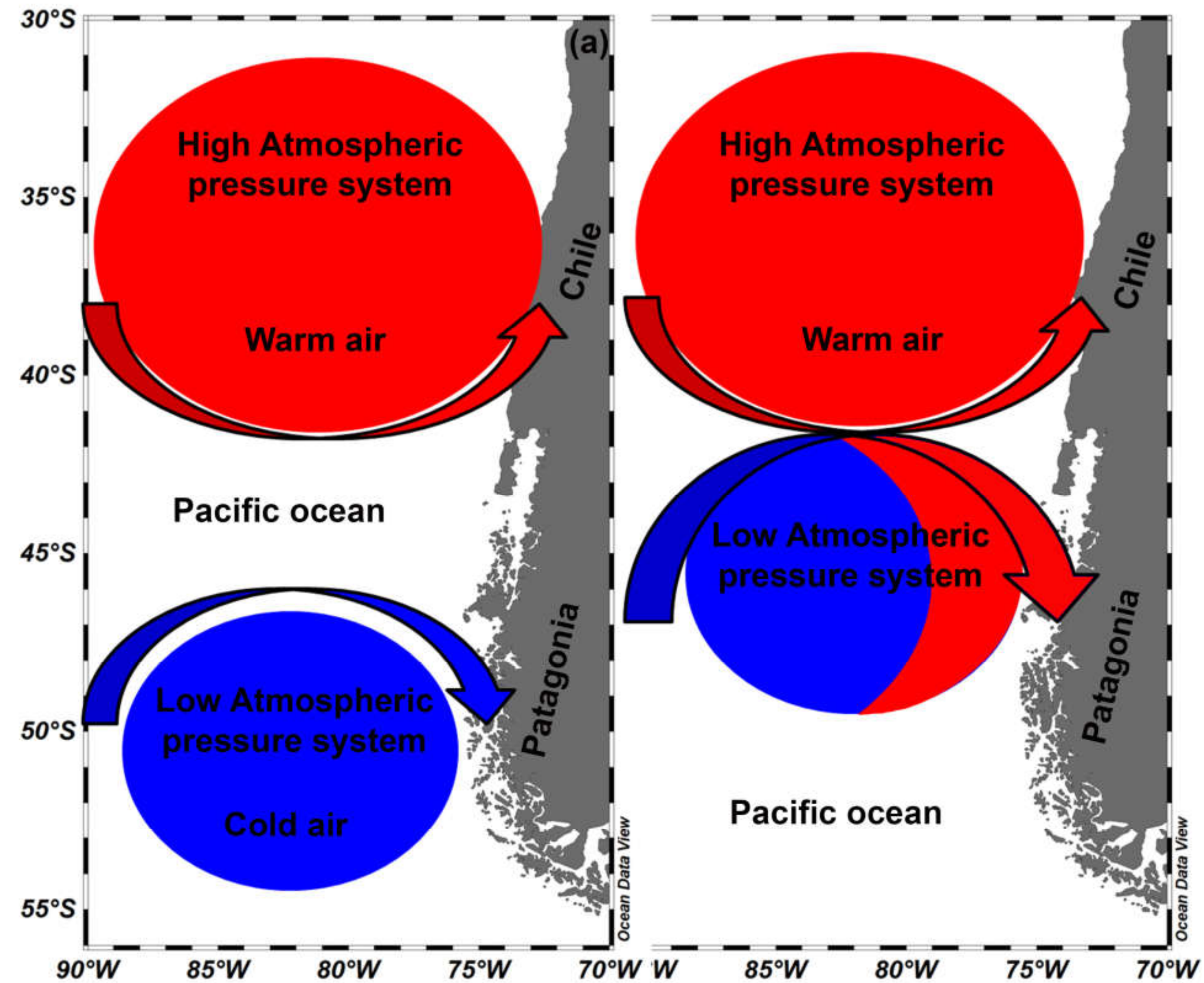

Figure 16. A conceptual model of the "Night-time heat wave event" in the Eastern Austral Pacific Ocean. (**a**) The initial condition, where a low atmospheric pressure system with cold air and a high atmospheric pressure system with warm air are regionally present, although separate; (**b**) the low atmospheric pressure system moves northward and encounters the high atmospheric pressure system, advecting warm air to Patagonia.